

DELFT UNIVERSITY OF TECHNOLOGY
AE4130 AIRCRAFT AERODYNAMICS



Assignments 1 to 5

Changkyu Park 4646061

February 8, 2021

Table of Contents

1 Assignment 1	1
1.1 Description of the solver	1
1.2 Verification using open literature	3
1.3 Comparison of airfoils with and without camber	4
1.4 Effect of panel density	5
1.5 Difference between thick and thin symmetrical airfoils	5
1.6 Difference in lift gradient of the thin and thick airfoils	7
1.7 Program made and used	8
2 Assignment 2	11
2.1 Airfoil analysis	11
2.1.1 Relationship between airfoil velocity distribution in the boundary layer and the pressure gradient over the airfoil	11
2.1.2 Determining airfoil to be used	12
2.1.3 Lift and drag polar	12
2.1.4 Shift in transition point	13
2.2 Airfoil improved design	15
2.2.1 Modified airfoil	15
2.2.2 Differences in performance	16
2.3 The laminar separation bubble	17
2.3.1 Explanation of effects of laminar separation bubble	17
2.3.2 Analysis of the NACA 2607 airfoil	17
2.3.3 Length of the bubble	18
2.3.4 Effect of the n -factor on the length of the separation bubble and drag coefficients, C_d	18
2.3.5 User defined transition locations	19
2.3.6 Critical roughness height	21
3 Assignment 3	22
3.1 Difference between leading-edge slat and trailing-edge flap	22
3.2 Main effects that determine the behaviour of a high lift system	22
3.2.1 Slat effect	22
3.2.2 Circulation effect	23
3.2.3 Dumping effect	23
3.2.4 Off-the-surface pressure recovery	24
3.2.5 Fresh boundary layer effect	24
3.3 Wake bursting	24
3.4 Relevant 2D-case of GA(W)-1 airfoil	26
3.4.1 Pressure field	28
3.4.2 Plain flap	29
3.4.3 Boundary layer effects	31
4 Assignment 4	38
4.1 Task 1	38
4.1.1 Relation between normalwash velocity and dihedral angle	38
4.1.2 Reason behind increase in aerodynamic performance with addition of winglets	39
4.2 Task 2	39
4.2.1 Initial plain wing	39
4.2.2 Inclusion of winglet	40
4.2.3 Variance of cant angle	41
4.2.4 Variance of verticle winglet height	42
4.3 Task 3	43
4.4 Task 4	44

5 Assignment 5	48
5.1 Part 1: The solver	48
5.1.1 Velocity diagram	48
5.1.2 Radial distribution of axial and tangential flow velocity	49
5.1.3 Induced axial velocity in the propeller plane vs far downstream in the slip-stream	49
5.1.4 Definitions used for propeller characteristics	50
5.1.5 Short explanations	50
5.2 Part 2: Analysis of a propeller	51
5.2.1 Propeller chosen	51
5.2.2 Comparison between BEM and experimental results	52
5.2.3 Axial velocity distribution	54
5.2.4 Effect of geometrical changes on efficiency	55
5.3 Source code used for the assignment	58
5.3.1 Blade Element Method for propeller 6623-A	58
References	62

1 Assignment 1

1.1 Description of the solver

The solver consists of 2 main parts. The first part is where the coordinates of the airfoil are given out using the airfoil model as an input. The second part then uses these coordinates to implement the thin airfoil theory and apply the discrete panel method, giving out lift coefficient, C_l , and pressure distribution, ΔC_p , at a given angle of attack, α . This is visualized using a flow diagram as shown in Figure 1.1.

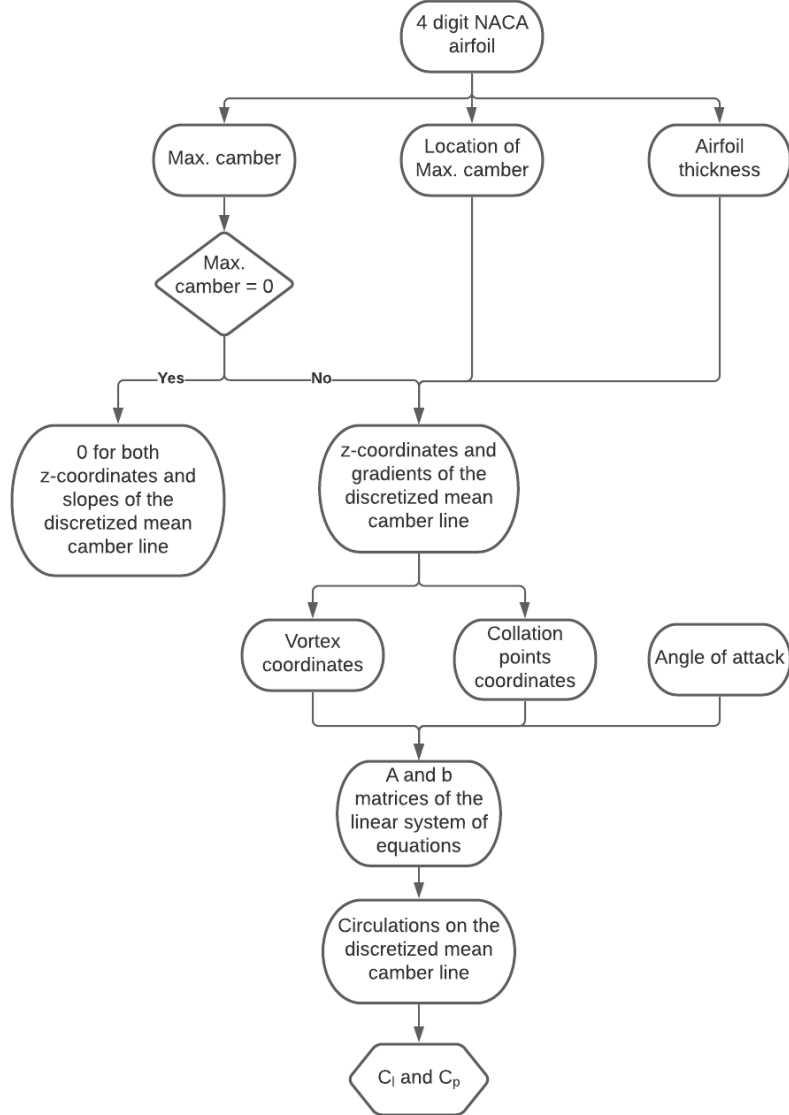


Fig. 1.1 Flow diagram of the solver

In the first part, the 4 digit NACA airfoil is fed into the program. Since the first digit represents the maximum camber as a percentage of the chord (m), the second digit represents the location of maximum camber with respect to leading edge divided by 10 (p) and the last 2 digits represent maximum airfoil thickness as a percentage of the chord, they can be used to calculate the coordinates of the discretized mean camber line and its gradients using the following equations provided by [1].

For calculating the coordinates:

$$y_c = \begin{cases} \frac{m}{p^2} \left(2p \left(\frac{x}{c} \right) - \left(\frac{x}{c} \right)^2 \right), & 0 \leq x \leq pc \\ \frac{m}{(1-p)^2} \left((1-2p) + 2p \left(\frac{x}{c} \right) - \left(\frac{x}{c} \right)^2 \right), & pc \leq x \leq c \end{cases} \quad (1.1)$$

For calculating the gradients:

$$\frac{dy_c}{dx} = \begin{cases} \frac{2m}{p^2} \left(p - \frac{x}{c} \right), & 0 \leq x \leq pc \\ \frac{2m}{(1-p)^2} \left(p - \frac{x}{c} \right), & pc \leq x \leq c \end{cases} \quad (1.2)$$

In the second part, a linear system of equations, $A\vec{x} = \vec{b}$, was set up as guided in [2]. The matrix A is an $N \times N$ matrix, where N is the number of elements in the discretized mean camber line. This A matrix comprises of the following elements, a_{ij} , where i represents the i^{th} row and j represents the j^{th} column.

$$a_{ij} = (u, w)_{ij} \cdot \mathbf{n}_i \quad (1.3)$$

where $(u, w)_{ij}$ is

$$\begin{pmatrix} u \\ w \end{pmatrix}_{ij} = \frac{1}{2\pi r_{ij}^2} \begin{pmatrix} 0 & 1 \\ -1 & 0 \end{pmatrix} \begin{pmatrix} x_i - x_j \\ z_i - z_j \end{pmatrix} \quad (1.4)$$

x_i and z_i are the x - and z -coordinate of the collocation point and x_j and z_j are that of the vortex. $(r_{ij})^2$ is

$$r_{ij}^2 = (x_i - x_j)^2 + (z_i - z_j)^2 \quad (1.5)$$

Furthermore, \mathbf{n}_i of (1.3) is

$$\mathbf{n}_i = (\sin \alpha_i, \cos \alpha_i) \quad (1.6)$$

where α_i is the angle the element of the mean camber line makes with the horizontal.

It is important to note the location of the collocation point and vortex on each discrete element of the mean camber line. Every collocation point is located at $3/4$ and every vortex is located at $1/4$ of every discrete element of the mean camber line with respect to the forward-most point of the element. This is also described in the following Figure 1.2.

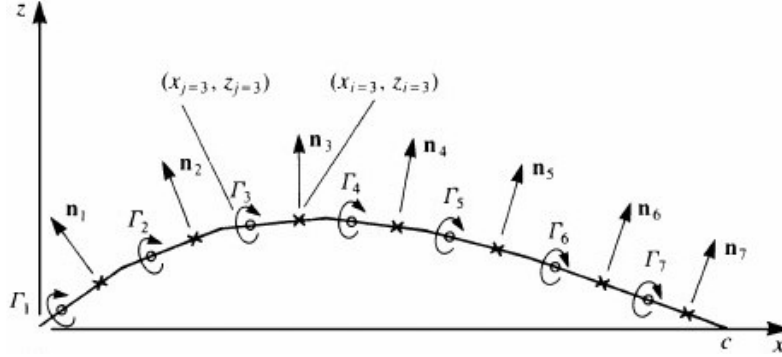


Fig. 1.2 Discretized mean camber line [2]

For the vector \mathbf{b} of the linear system of equations, the elements of the vector, b_i , are as follows:

$$b_i = -Q_\infty [\sin(\alpha + \alpha_i)] \quad (1.7)$$

where Q_∞ is the free stream velocity.

Solving the linear system of equations, we get the values for elements of vector \vec{x} , Γ_i , which represents the vortex at each of the discretized element that is visualised in Figure 1.2.

1.2 Verification using open literature

In verifying the program created, two different sets of data have been used. First is a simulation data from NASA Langley Research Center and the other is an experimental data from North Atlantic Treaty Organization Advisory Group For Aerospace Research and Development (AGARD). Both data are based on NACA 0012 airfoil which is considered thin and for NASA's data, angle of attack, α , of 10 degrees was used for comparison [3] and for AGARD's data, $\alpha = 2$ degrees was used [4]. The data of pressure coefficients, C_p , used had to be treated in another Python program to plot the values of ΔC_p . The following plots were then produced.

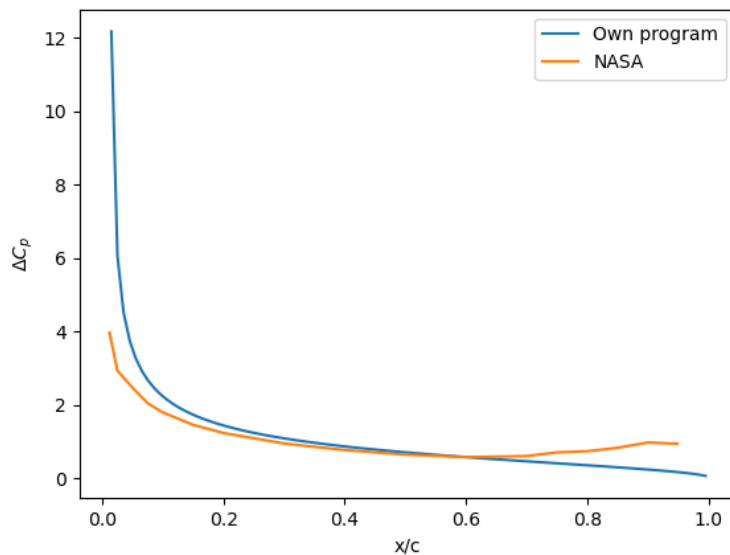


Fig. 1.3 Comparison against NASA's data for $\alpha = 10^\circ$

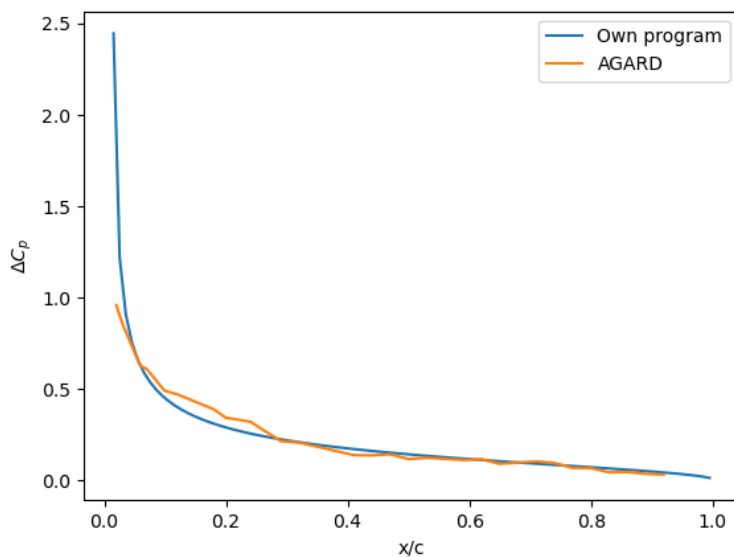


Fig. 1.4 Comparison against AGARD's data for $\alpha = 2^\circ$

From Figures 1.3 and 1.4, it can be observed that the program created describes the difference in pressure distribution fairly well, especially at a lower angle of attack of $\alpha = 2^\circ$ in which the thin airfoil theory is known to work well for. At $\alpha = 10^\circ$ which is closer to the limiting value of angle of attack for thin airfoil theory, the program does not describe NASA's simulation data too well. However, the general shape still matches, verifying the performance of the program.

1.3 Comparison of airfoils with and without camber

As for the comparison between a symmetrical airfoil and a cambered airfoil, NACA 2412 were chosen as the cambered. It is to be noted that as for the symmetrical airfoil, the airfoil is treated as a thin one regardless of the model number. The choice was made based on a small enough thickness of the cambered airfoil, described by the last 2 digits of the model name. The comparison for their lift coefficients and difference in pressure coefficients are shown in Figure 1.5 and 1.6.

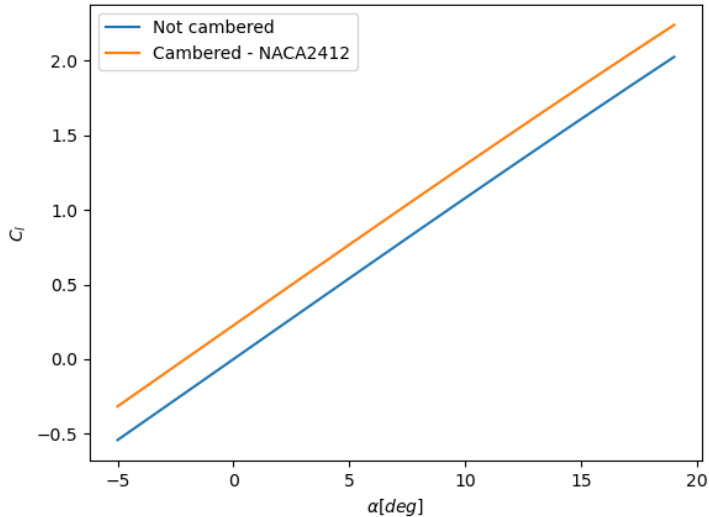


Fig. 1.5 C_l comparison of airfoil with and without camber

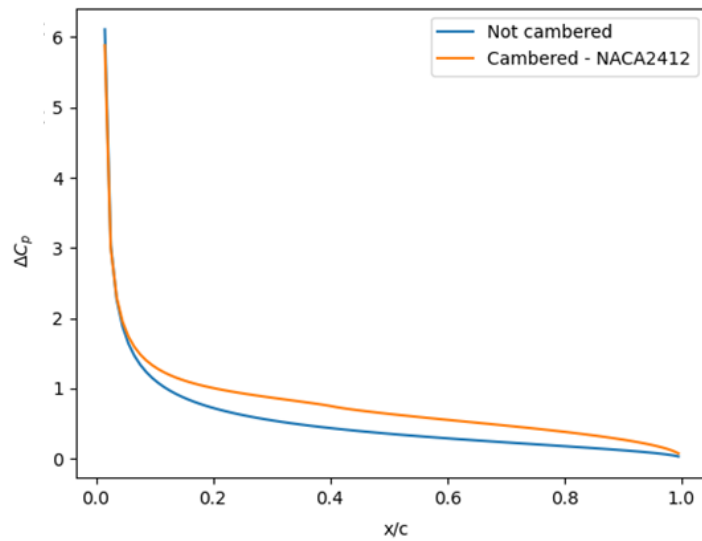


Fig. 1.6 ΔC_p comparison of airfoil with and without camber

Firstly for C_l plot of Figure 1.5, it can be seen from both the linear lines that there is no stall due to the limitations of the program created. Secondly, it can be observed that the cambered airfoil can produce more lift at each angle of attack than the non-cambered airfoil and that this lift is non-zero at $\alpha = 0$ which was an expected outcome for the cambered airfoil while the lift is zero for $\alpha = 0$ for the non-cambered symmetrical airfoil.

For the ΔC_p plot, the difference comes mainly from the bottom part of the graph. It is clear that the cambered airfoil possesses a larger difference in pressure of the upper and lower side of the airfoil than the non-cambered airfoil. This is due to the much larger negative pressure coefficient on the suction (upper) side of the cambered airfoil compared to that of the non-cambered airfoil.

1.4 Effect of panel density

The following Figure 1.7 shows the difference in the analysis of the difference in pressure coefficient for the different number of panels. All the curves have fairly similar behaviour towards the trailing edge of the airfoil. However, the difference gets much more significant towards the leading edge. The larger the number of panels, the quicker the difference drops (steep part of the curve), leading to a shallow curve.

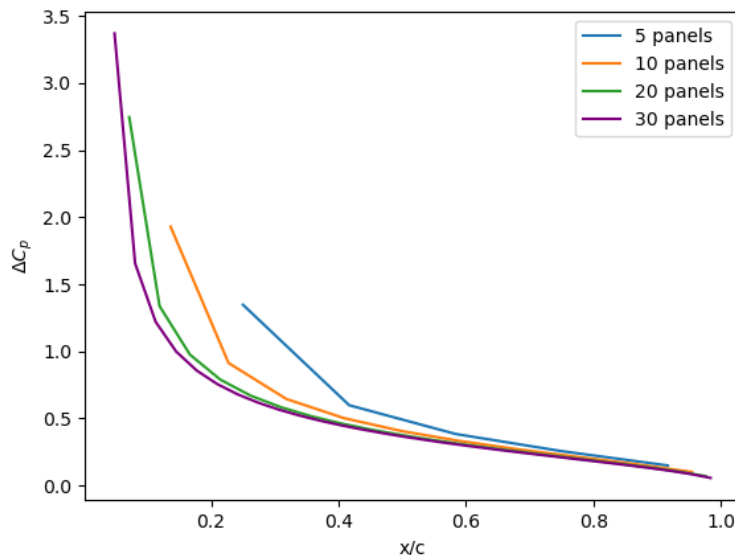


Fig. 1.7 ΔC_p comparison between different number of panels

The higher the number of the panels, the better it is. However, the minimum number of panels I would recommend is 20 or even 25 as it can be seen that even 20 panels show a clear deviation away from 30 panels.

1.5 Difference between thick and thin symmetrical airfoils

The given data of thick airfoil in the table was used to calculate ΔC_p for $\alpha = 0$ and 5 degrees. This was then compared against the data that my program produced which was for the thin airfoil. These were then plotted as shown in Figures 1.8 and 1.9 for $\alpha = 0$ and 5 degrees respectively. Beginning with the comparison at $\alpha = 0$ degree in Figure 1.8, the two lines completely overlap each other (hence the blue line is not visible) in the entire domain of x/c . Thus, it can be concluded that there is no difference between the thin and thick airfoils for $\alpha = 0$ degree. As for Figure 1.9 that compares the thin and thick airfoils at $\alpha = 5$ degree, some visible difference can be seen.

At the leading edge, the thin airfoil's ΔC_p rises to a high value which in this case is around 6 whereas for the thick airfoil, it goes to almost 0. This difference comes from the fact that thick airfoil has two surfaces, top and bottom that cancel each other out whereas, for the thin airfoil, this is not accounted for. Additionally, there is a difference in magnitude of ΔC_p from leading edge to around $x/c = 0.6$. The thick airfoil has a higher value in this region since it has a non-zero thickness which allows for creating a higher pressure in its lower airfoil surface and lower pressure in its upper surface.

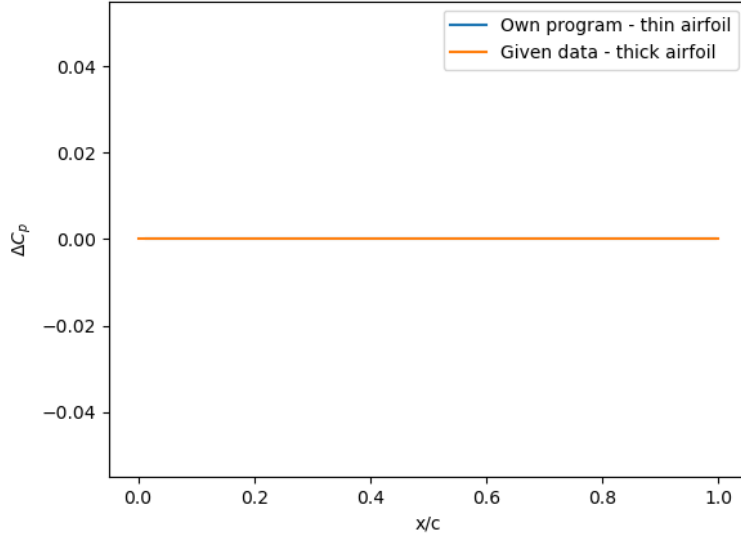


Fig. 1.8 Comparison between thin symmetrical airfoil and thick NACA 0015 airfoil for $\alpha = 0^\circ$

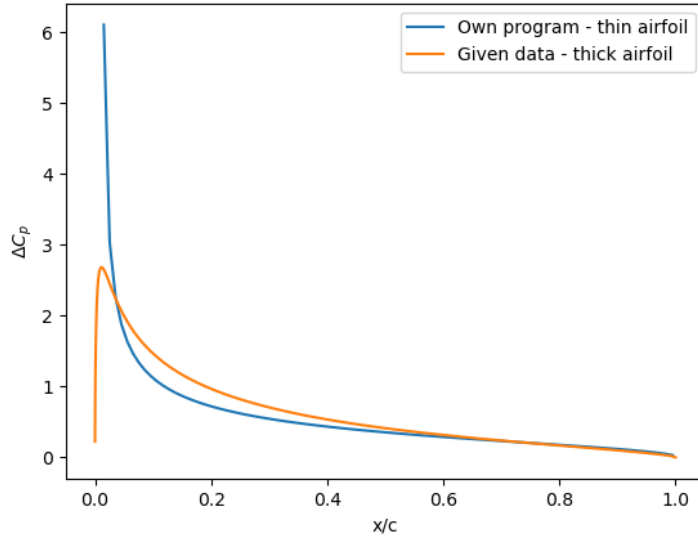


Fig. 1.9 Comparison between thin symmetrical airfoil and thick NACA 0015 airfoil for $\alpha = 5^\circ$

1.6 Difference in lift gradient of the thin and thick airfoils

Before diving into the calculation method, the following Table 1.1, has been produced which records the lift gradients, $C_{l\alpha}$ of the thin symmetrical airfoil and thick NACA 0015 airfoil, the data for which is provided in the assignment. The thick airfoil has a greater $C_{l\alpha}$ value compared to the thin airfoil.

Table 1.1 Comparison of lift gradients of thin symmetrical airfoil and thick NACA 0015 airfoil

	thin	thick
$C_{l\alpha}$	0.10221	0.12299

This is an expected outcome and it confirms the theory Sighard Hoerner claims in [5] whereby the lift gradient is described by (1.8). The exact value that the equation gives is not compared to the values of Tabler 1.1 due to the difference in modelled and experimental analyses.

$$c_{L\alpha} \approx 0.11 + 0.09 \cdot \frac{t}{c} \quad (1.8)$$

Moving onto the explanation of the calculation method. Firstly, lift, L , is a force and is calculated using the pressure difference between the upper and lower surfaces of the airfoil which is the ΔC_p that has been constantly used in this report. The exact relationship between them is described by (1.9).

$$L = \Delta C_p \cdot \text{surface area} \quad (1.9)$$

$$= \int \Delta C_p \cdot d\left(\frac{x}{c}\right) \cdot \text{chord length} \cdot \text{span} \quad (1.10)$$

In this analysis, unit chord length and unit span are used. Thus, only the integral needs to be calculated for. The following Figure 1.10 is used for the explanation of how the integral is calculated.

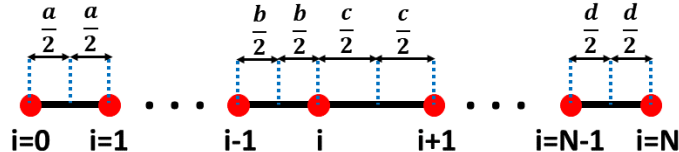


Fig. 1.10 Discretization of airfoil

For both the provided data of thick NACA0015 airfoil and the thin symmetrical airfoil the program calculates for, the airfoil is discretized into N number of nodes, so $i = 0, 1, 2, \dots, N-1, N$. Furthermore, we have the values of ΔC_p at each of these nodes. Thus, in order to calculate the integral, these values of ΔC_p have to multiplied by certain length segments of the airfoil. As for the first node, $i = 0$, due to the absence of extra node outside the airfoil, the ΔC_p value at this node is multiplied by half the distance between $i = 0$ and $i = 1$, $1/2$, as seen in Figure 1.10. This goes the same for the node $i = N$ which only uses the point $i = N - 1$. As for the rest of the nodes between, 2 other nodes are utilised for every node giving total distance of $(b/2 + c/2)$ for node i as shown in the same figure.

1.7 Program made and used

```
1 import numpy as np
2 import matplotlib
3 import matplotlib.pyplot as plt
4
5 def NACA4digits(model, linetype="camber"):
6     """
7         Parameters
8         -----
9         model : string
10            4 digit model number of a NACA airfoil
11            linetype : string, optional
12                Can be "camber" for camberline calculation and "slope" for slope
13                calculation. The default is "camber".
14
15         Returns
16         -----
17         function
18             This function relates coordinates (x,z) of linetype
19
20         """
21     m = float(model[0]) / 100 # max camber [%]
22     p = float(model[1]) / 10 # location of max camber [%]
23     t = float(model[2:]) / 100 # airfoil thickness [%]
24
25     if m == 0 or p == 0: # Symmetrical airfoil
26         return lambda xc : 0
27
28     elif linetype == "camber":
29         return np.vectorize( lambda xc : m/(p**2)*(2*p*xc-xc**2) if xc <= p
30                             else m/( (1-p)**2 ) * ( (1-2*p) + 2*p*xc - xc**2 ) )
31
32     elif linetype == "slope":
33         return np.vectorize( lambda xc : m/(p**2)*(2*p-2*xc) if xc <= p else
34                             m/( (1-p)**2 ) * ( 2*p - 2*xc ) )
35
36 def func2coord(func, k):
37     """
38         Parameters
39         -----
40         func : function
41             Equation that relates x and z coordinates of camberline or slope
42         k : int
43             Number of nodes on the airfoil
44
45         Returns
46         -----
47         coord : tuple of arrays
48             2 arrays containing x and z coordinates of the camberline or slope
49
50         """
51     xc = np.linspace(0,1,k)[1:] # First point (x/c = 0) is excluded to avoid
52     division by 0 in subsequent calculations
```

```

50     coord = np.zeros((np.size(xc),2))
51     coord[:,0] = xc
52     coord[:,1] = func(xc)
53
54     return coord
55
56
57 def potential_flow(coord, alpha):
58     """
59     Parameters
60     -----
61     coord : tuple of arrays
62         2 arrays containing x and z coordinates of the camberline or slope
63     alpha : angle of attack
64         unit is radians
65
66     Returns
67     -----
68     c_l : float
69         Lift coefficient at this specific angle of attack
70     xc : array of floats
71         x coordinates for which values of Delta_c_p are allocated
72     Delta_c_p : array of floats
73         Difference in pressure coefficients
74
75     """
76     n = coord.shape[0]-1 # number of panels = number of nodes - 1
77     coord_x = coord[:,0] # x coordinates
78     coord_z = coord[:,1] # z coordinates
79
80     # normal vectors
81     slopes = (coord_z[1:] - coord_z[:-1]) / (coord_x[1:] - coord_x[:-1]) #
82     # gradients of the camberline
83     incl = -1*np.tan(slopes) # inclination angle in radians
84     normal = np.zeros((n,2))
85     normal[:,0] = np.sin(incl)
86     normal[:,1] = np.cos(incl)
87
88     # vortex coordinates
89     vortex_coord = np.zeros((n,2))
90     vortex_coord[:,0] = (coord_x[1:] - coord_x[:-1]) * 0.25 + coord_x[:-1]
91     vortex_coord[:,1] = (coord_z[1:] - coord_z[:-1]) * 0.25 + coord_z[:-1]
92
93     # collocation points coordinates
94     col_coord = np.zeros((n,2))
95     col_coord[:,0] = (coord_x[1:] - coord_x[:-1]) * 0.75 + coord_x[:-1]
96     col_coord[:,1] = (coord_z[1:] - coord_z[:-1]) * 0.75 + coord_z[:-1]
97
98     # linear system
99     A = np.zeros((n,n))
100    b = np.zeros((n))
101    transform = np.array([[0,1], [-1, 0]])
102    coeff = 1 / (2 * np.pi) * transform
103
104    # Outer for loop loops around collocation points
105    # Inner for loop loops around vortex coordinates

```

```

105     for i in range(n):
106         xi, zi = col_coord[i,0], col_coord[i,1]
107         for j in range(n):
108             xj, zj = vortex_coord[j,0], vortex_coord[j,1]
109             r2 = (xi-xj)**2 + (zi-zj)**2
110             A[i,j] = np.dot(coeff/r2 @ np.array([xi-xj,zi-zj]), normal[i,:])
111             b[i] = -np.sin(alpha + incl[i])
112
113     circulation = np.linalg.solve(A,b)
114
115     c_l = np.sum(circulation) * 2 # Lift coefficient calculation
116
117     Delta_c = coord_x[1:] - coord_x[:-1] # Panel length
118     Delta_c_p = 2 * circulation / Delta_c # Pressure coeff difference
119     xc = (coord_x[1:] - coord_x[:-1]) * 0.5 + coord_x[:-1] # new x coordinates
120     # for which values of Delta_c_p are allocated
121
122     return c_l, xc, Delta_c_p
123
124
125     ''' C_l calculation '''
126     airfoil_model = "0015"
127     coord = func2coord(NACA4digits(airfoil_model),100)
128
129     alpha = np.radians(np.arange(0, 5, 1)) # Array of angle of attack we want to
130     # calculate for
131     c_l = []
132
133     # Loop through the potential_flow function to obtain lift coefficient at
134     # different angle of attacks
135     for i in alpha:
136         c_l.append(potential_flow(coord,i)[0])
137
138
139     ''' C_p calculation '''
140     AOA = 5 # Angle of attack in degrees
141     alpha = np.radians(AOA) # Convert angle of attack to radians
142     xc = potential_flow(coord,alpha)[1] # x coordinate for Delta_c_p location
143     Delta_c_p = potential_flow(coord,alpha)[2]
144
145     ''' Plotting '''
146     fig1, ax1 = plt.subplots()
147     ax1.set_xlabel('x/c')
148     ax1.set_ylabel('$\Delta C_p$')
149     ax1.plot(xc, Delta_c_p)
150     plt.show()

```

2 Assignment 2

2.1 Airfoil analysis

2.1.1 Relationship between airfoil velocity distribution in the boundary layer and the pressure gradient over the airfoil

The Prandtl boundary layer equation for 2-dimensional flow is as follows

$$\rho u \frac{\partial u}{\partial x} + \rho v \frac{\partial u}{\partial y} = \rho_e u_e \frac{du_e}{dx} + \mu \frac{\partial^2 u}{\partial y^2} \quad (2.1)$$

where ρ : flow density, u : flow velocity in x-direction, v : flow velocity in y-direction, μ : dynamic viscosity and the subscript e stands for the edge of the boundary layer.

We then apply the following boundary condition at the wall:

$$\text{at } y = 0 : u = 0 \quad v = 0 \quad (2.2)$$

which then simplifies (2.1) into

$$0 = \rho_e u_e \frac{du_e}{dx} + \mu \left(\frac{\partial^2 u}{\partial y^2} \right)_{y=0} \quad (2.3)$$

Using the Euler equation, (2.3) becomes

$$0 = \rho_e u_e \frac{du_e}{dx} + \mu \left(\frac{\partial^2 u}{\partial y^2} \right)_{y=0} \quad (2.4)$$

$$0 = -\frac{dp}{dx} + \mu \left(\frac{\partial^2 u}{\partial y^2} \right)_{y=0} \quad (2.5)$$

$$\mu \left(\frac{\partial^2 u}{\partial y^2} \right)_{y=0} = \frac{dp}{dx} \quad (2.6)$$

$$\nu \left(\frac{\partial^2 u}{\partial y^2} \right)_{y=0} = \frac{1}{\rho} \frac{dp}{dx} \quad (2.7)$$

where p : pressure, ν : kinematic viscosity and $\mu = \nu \rho$. We have now achieved the First Compatibility Equation (FCE) which is (2.7).

This tells us that on the boundary layer (wall, $y = 0$), when the pressure decreases ($dp/dx < 0$), the velocity profile is convex as shown in Fig.2.1 and when the pressure increases ($dp/dx > 0$), the velocity profile is concave as shown in Fig.2.2. Furthermore, at the location where pressure is minimum ($dp/dx = 0$), the velocity profile is straight as shown in Fig.2.3.

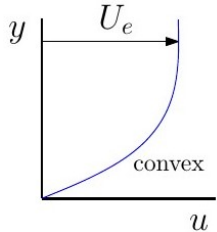


Fig. 2.1 $y - u$ plot for $dp/dx < 0$ [6]

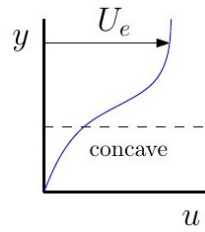


Fig. 2.2 $y - u$ plot for $dp/dx > 0$ [6]

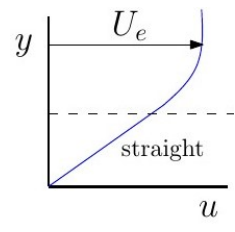


Fig. 2.3 $y - u$ plot for $dp/dx = 0$ [6]

2.1.2 Determining airfoil to be used

The following are the steps taken to determine the airfoil that is assigned to me

- My student number is 4646061.
- Its last 3 digits are 061.
- The sum of these 3 digits is $0 + 6 + 1 = 7$
- Hence, the last 2 digits of my NACA airfoil is 07.
- The second digit of my student number is 6.
- So, the second digit of my NACA airfoil is 6.
- I am assigned to NACA 2607 airfoil

This assigned NACA 2607 airfoil is visualised in Fig.2.4.

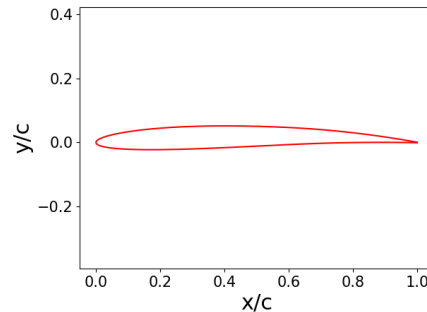


Fig. 2.4 Assigned airfoil - NACA 2607

2.1.3 Lift and drag polar

The following plots of lift and drag polar were obtained using $\text{Re} = 0.8 \times 10^6$ and $\text{Mach} = 0$ as instructed.

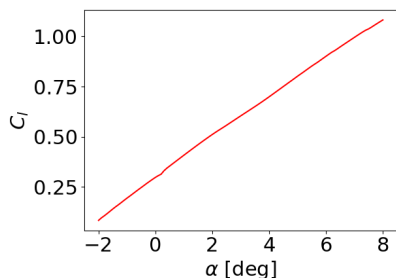


Fig. 2.5 Lift polar plot of NACA 2607

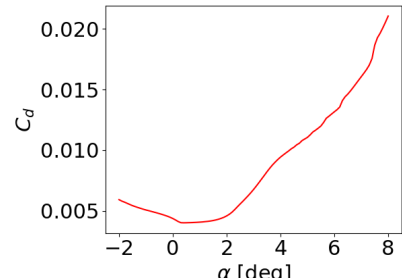


Fig. 2.6 Drag polar of NACA 2607

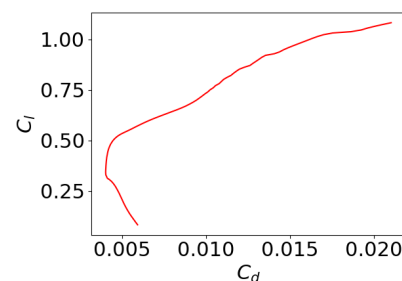


Fig. 2.7 Lift-drag polar of NACA 2607

2.1.4 Shift in transition point

In order to observe the change in chordwise location of the transition point with respect to angle of attack, the pressure coefficient distributions at the various angles of attack are plotted and is shown in Fig.2.8.

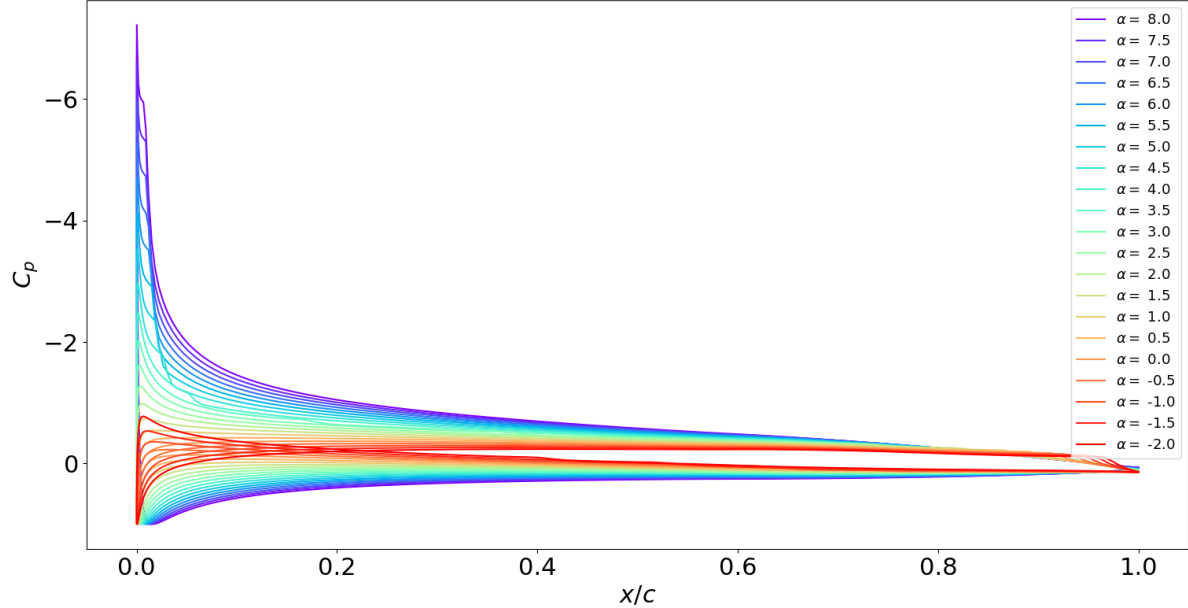


Fig. 2.8 Pressure coefficient, C_p , distribution on NACA 2607

In order to better observe this change, zoomed-in plots with C_p of only the upper surface has been produced as shown in Fig.2.9, 2.10 and 2.11 with all the transition points labelled. These transition points are identified by finding the adverse pressure gradients of each curve.

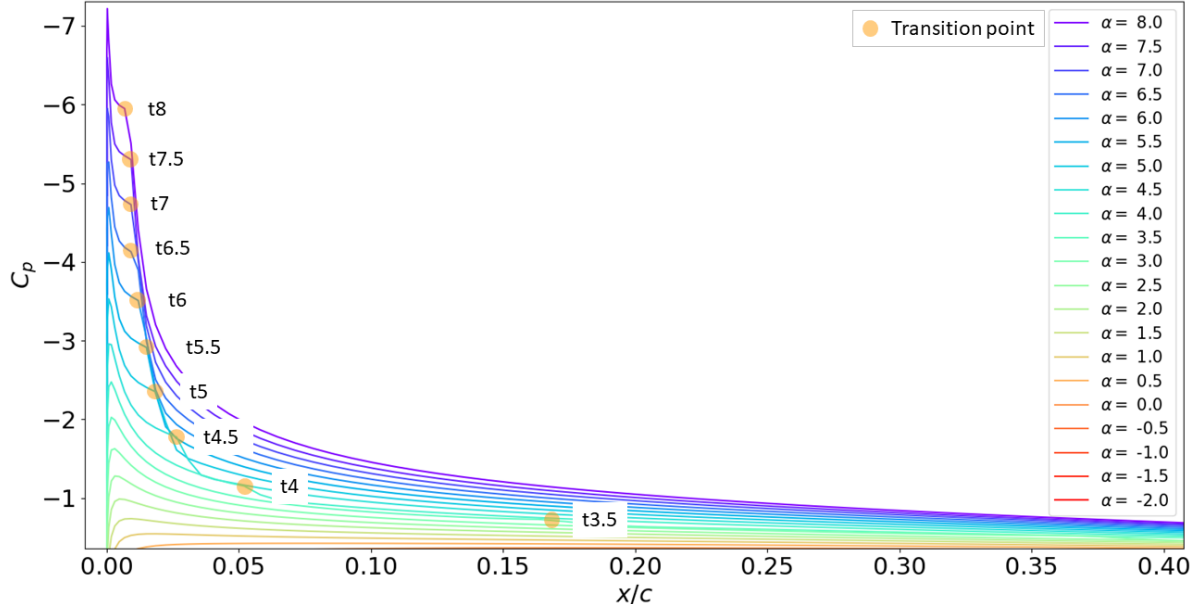


Fig. 2.9 Pressure coefficient, C_p , distribution on upper surface of NACA 2607 - part a

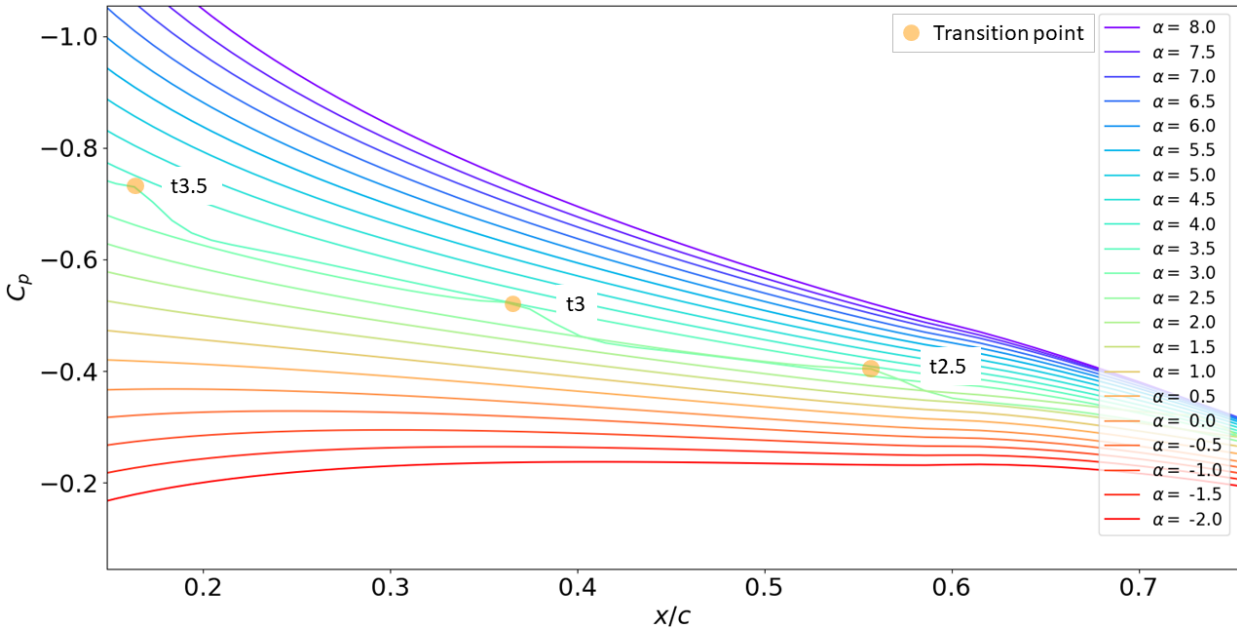


Fig. 2.10 Pressure coefficient, C_p , distribution on upper surface of NACA 2607 - part b

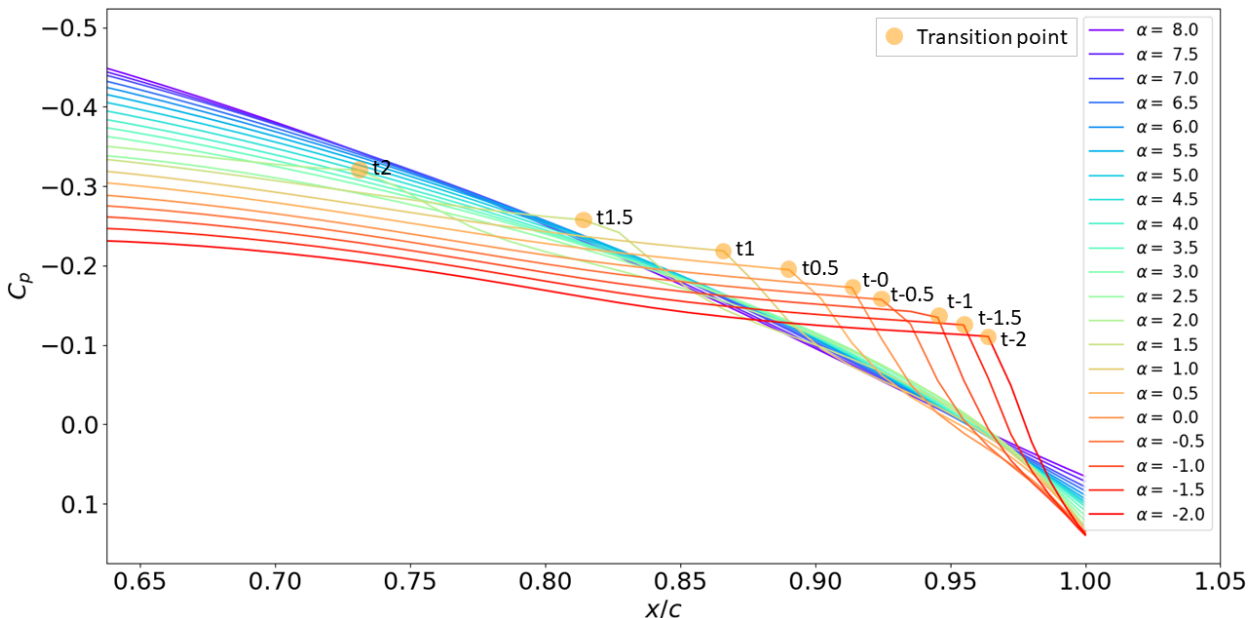


Fig. 2.11 Pressure coefficient, C_p , distribution on upper surface of NACA 2607 - part c

The transition point for each angle of attack has been marked with orange circles. It can be realised that the transition point gradually moves aft until $\alpha = 4$ where this backward shift starts to exponentially increase as shown in Fig.2.9. This shift then exponentially decreases from $\alpha = 4$ as shown in Fig.2.11.

In general, it can be said that transition point moves chordwise, at a lower pressure coefficient, C_p , value for every decrease in angle of attack, α . Furthermore, the change in pressure gradients starts at a large value for $\alpha = 8$, decreases till $\alpha = 2.5$ and starts increasing again.

2.2 Airfoil improved design

At $C_l = 0.5$, $C_l/C_d = 111.879$ and this is obtained from the data that was used to produce Fig.2.6.

2.2.1 Modified airfoil

Using inverse airfoil design routines in XFOIL, a modified airfoil was produced which has a higher C_l/C_d than the original airfoil while maintaining the same relative thickness, t/c , and it is shown in Fig.2.12.

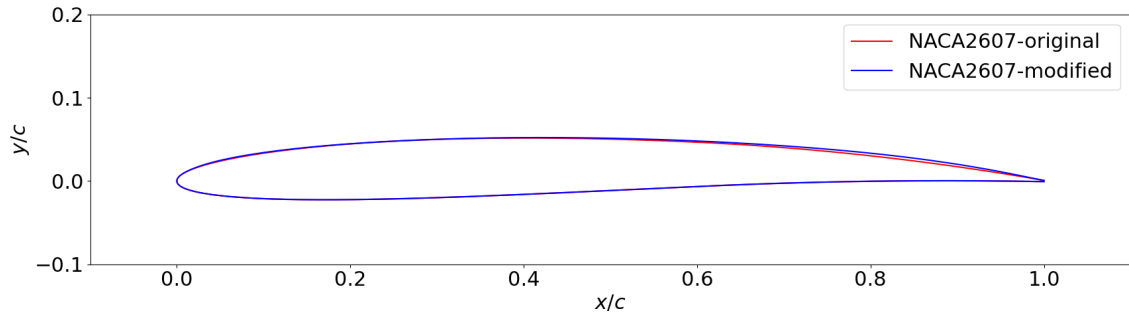


Fig. 2.12 Modified airfoil

The C_l/C_d of this modified airfoil at $C_l = 0.5$ is $C_l/C_d = 120.435$ which is a commendable improvement from the original airfoil. Table 2.1 was produced for easier comparison and it was realised that the modified airfoil has approximately 8% performance increase.

Table 2.1 Lift drag ratio comparison at $C_l = 0.5$

	C_l/C_d
Original airfoil	111.879
Modified airfoil	120.435

I focused on increasing the thickness behind the point of maximum thickness to increase the velocity over the upper surface. This was done by imposing the change on the upper surface of the airfoil between $x/c = 0.3$ and $x/c = 1.0$ as it can be seen in Fig.2.12. Furthermore, I have also attempted to increase the sharpness of the leading edge by pushing in the contour of the lower surface as this decreases the velocity over the lower surface of the airfoil. Lastly, the thickness near the leading edge around $x/c = 0.1$ was increased by pushing out the contour of the upper surface as this increases the velocity over the upper surface of the airfoil. All of these 3 modifications increase the C_l of the airfoil at a specific angle of attack.

This modification was done with the help of **MDES** function in XFOIL which allows for modification of the velocity of the surfaces using the plot $q/V_\infty - x/c$ in which the curves can be modified by the user by the function **MODI**. Thus, I have modified the plot to have a higher velocity on the upper airfoil surface and a lower velocity on the lower airfoil surface.

Most importantly, to not alter the relative maximum thickness, t/c , **MARK** function was used to specify the range within the airfoil surface that is to be altered. In this way, modification of both the upper and lower surface of point of the maximum thickness ($x/c = 0.3$ for this airfoil) could be prevented as shown in Fig.2.12.

2.2.2 Differences in performance

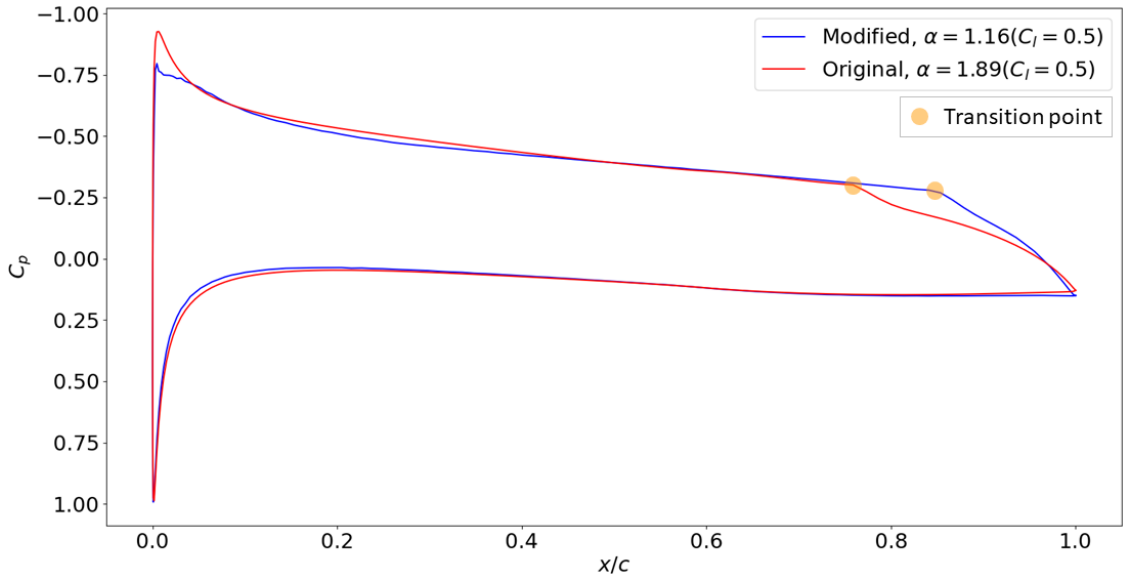


Fig. 2.13 Pressure distribution comparison of original and modified airfoils

An obvious feature that can be seen from Fig.2.13 is that for the modified airfoil, the transition point is delayed and is placed much further behind compared to that of the original airfoil. This shows that the amount of laminar flow is definitely increased.

The optimized (modified) airfoil and the original airfoil were also compared for the angle of attack of $\alpha = 10^\circ$ as show in Table 2.2. The optimized (modified) airfoil still performs better than the original counterpart for this angle of attack. However, it can be seen that the difference in value has decreased compared to values in Table 2.1. Thus, for an even higher angle of attack $\alpha > 10^\circ$, there is a high possibility that the original airfoil outperforms the optimized (modified) airfoil.

Table 2.2 Lift drag ratio comparison at $\alpha = 10^\circ$

	C_l/C_d
Original airfoil	28.508
Modified airfoil	30.512

2.3 The laminar separation bubble

2.3.1 Explanation of effects of laminar separation bubble

The laminar separation bubbles affect performances of airfoils to a large extent. They form when flow transition occurs downstream of the position of flow separation and the turbulent flow reattaches to the airfoil surface. This separation bubble thickens the boundary layer around the airfoil and significantly increases the drag the airfoil experiences. The difference in skin friction coefficient, C_f , and pressure coefficient, C_p , between flows over the upper surface of airfoils with and without the laminar separation bubble is shown in the following Fig.2.14.

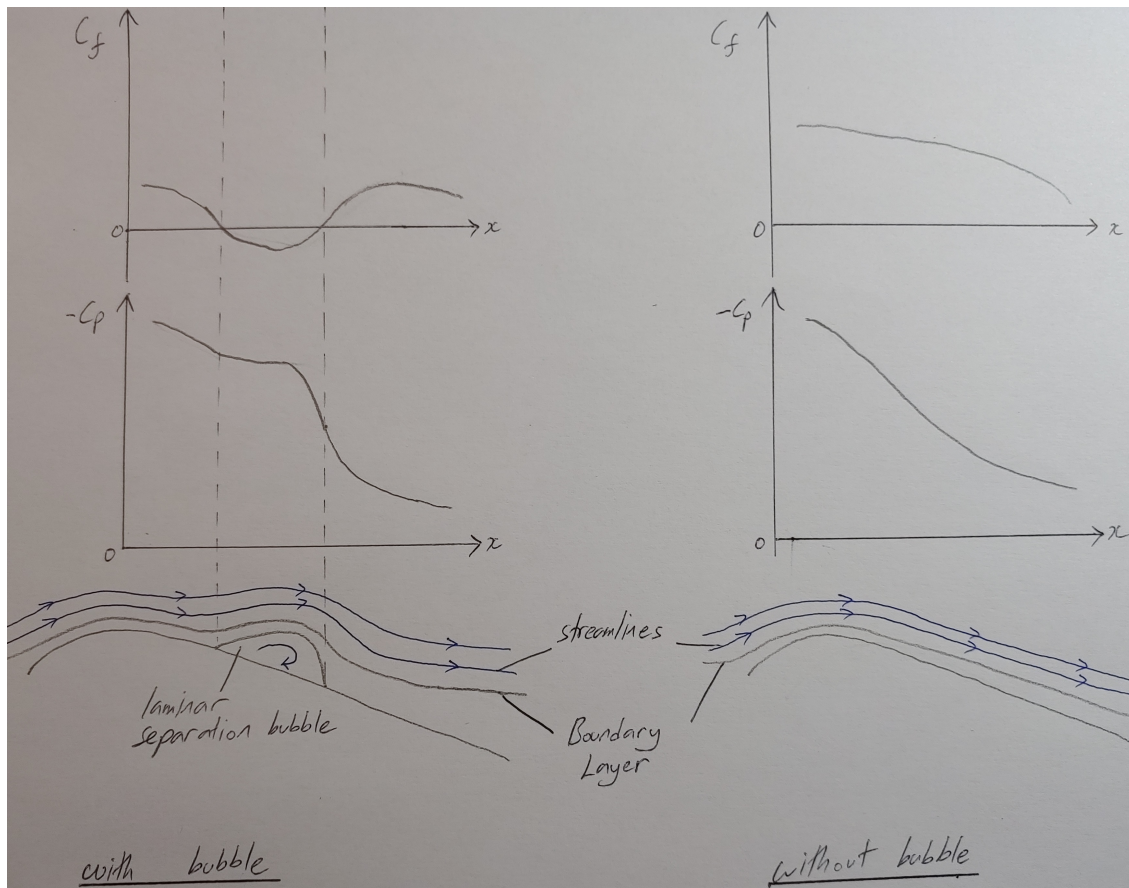


Fig. 2.14 Comparison between flows over airfoil upper surface with and without laminar separation bubble

2.3.2 Analysis of the NACA 2607 airfoil

The following Fig.2.15 describes the pressure distribution over NACA 2607 airfoil at a low Reynolds number of $5e5$. In this figure, the effect of the laminar separation bubble on the pressure distribution is clearly shown between $x/c = 0.85$ and 0.9 and is circled in red.

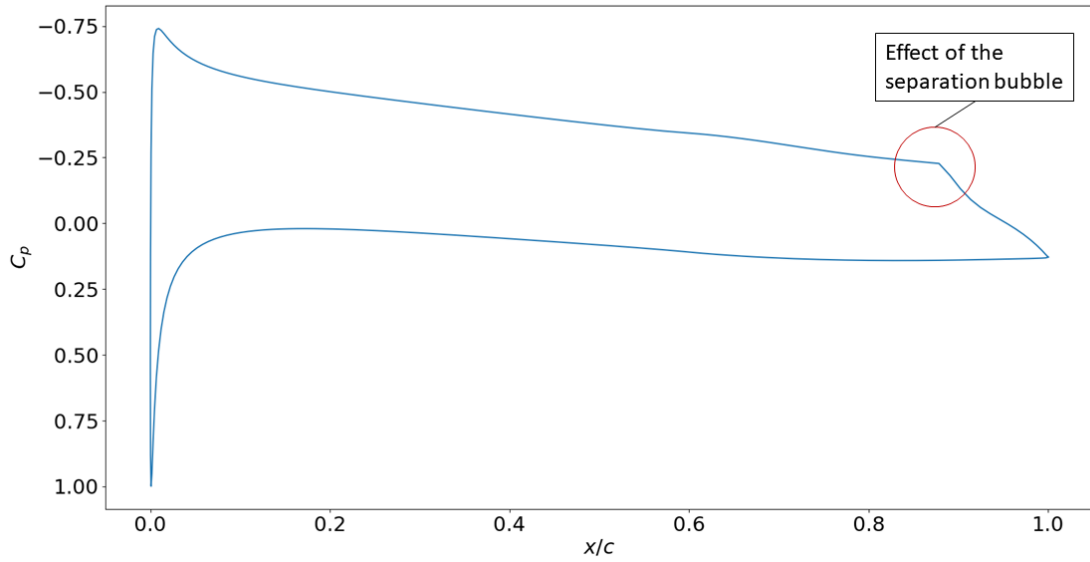


Fig. 2.15 Pressure distribution over NACA 26076 airfoil at $Re = 5 \times 10^5$ and $\alpha = 1.5^\circ$

2.3.3 Length of the bubble

The length of the laminar separation bubble is determined by the distance of the reattachment point with respect to the separation point and this depends on where the transition occurs [7]. At a large value of Reynolds number above a certain critical value, the flow is unstable. This instability in the flow induces transition near the separation point and thus the reattachment occurs early, forming a small separation bubble. On the other hand, when the Reynolds number is below the critical value, the flow is initially laminar downstream of the separation point. Instability gradually develops in the flow due to the change in the shape of the velocity profile, ultimately transitioning into turbulence, after which reattachment occurs, forming the longer separation bubble. The duration in which the flow stays laminar lengthens with even lower Reynolds number and thus, even longer bubbles form.

2.3.4 Effect of the n -factor on the length of the separation bubble and drag coefficients, C_d

Firstly, the effect on the pressure distribution is shown in Fig.2.16 where n-factors of 4, 6, 8, 10 and 12 are plotted and colour-coded.

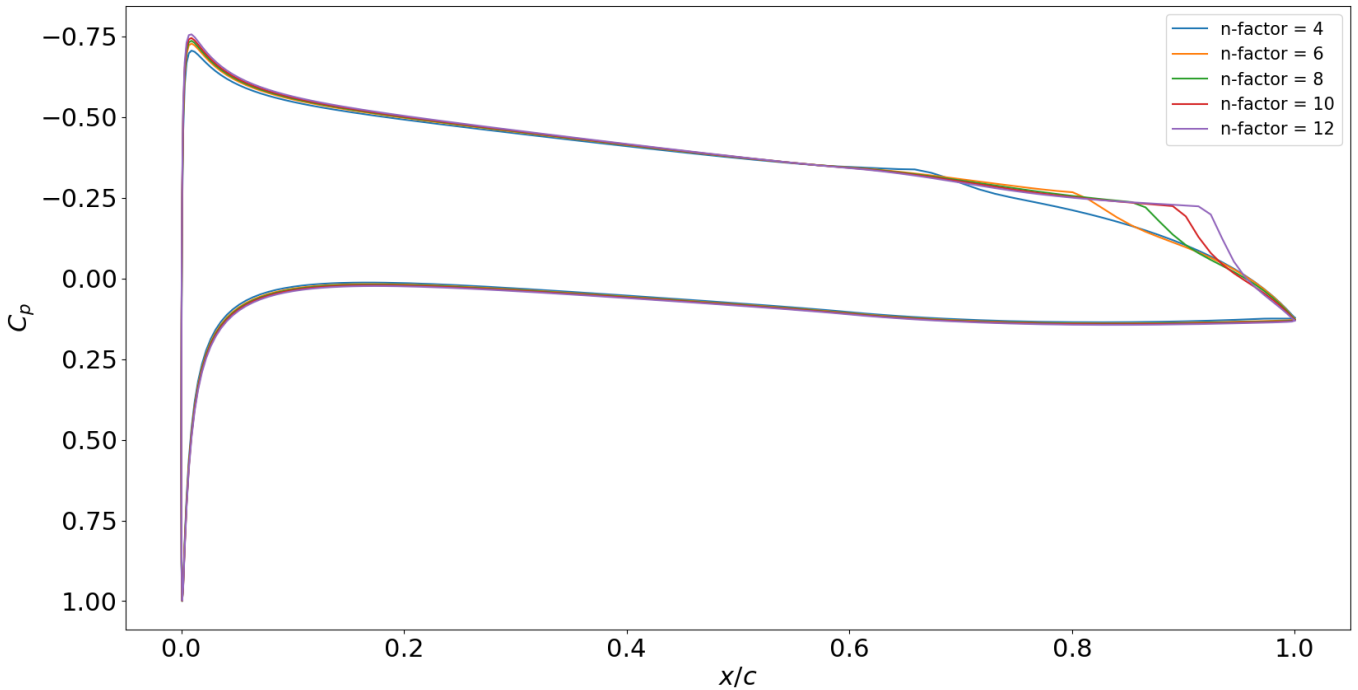


Fig. 2.16 Effect of the n -factor on pressure distribution at $Re = 5 \times 10^5$ and $\alpha = 1.5^\circ$

It can be clearly observed that length of the laminar separation bubble increases with the increase in value of n -factor.

The effect on the drag coefficient is described in the following Table 2.3.

Table 2.3 Effect of the n -factor on drag coefficient, C_d , at $C_l = 0.5$ and $Re = 5 \times 10^5$

n-factor	4	5	6	7	8	9	10	11	12
C_d	0.00711	0.00637	0.00566	0.00536	0.00525	0.00524	0.00527	0.00535	0.00549

As n -factor increases, the C_d decreases until n -factor= 9 at which C_d starts to increase instead.

Since lower n -factor relates to more turbulent inflow and higher value relates to less turbulent (so laminar) inflow. From Fig.2.16 and Table 2.3, it can be realised that at a very high n -factor where the flow is less turbulent, the drag is dominated by the laminar separation bubble. As n -factor decreases, so as inflow becomes more turbulent, the length of bubble decreases as shown in Fig.2.16 and thus the drag decreases as shown in Table 2.3. However, from n -factor of 9, further reduction in n -factor increases drag. This can be due to the turbulent boundary layer dominating the drag instead of the bubble.

For a low-speed aircraft, it can be said that a certain amount of turbulence in the inflow is appreciated for maximum efficiency. According to the XFOIL user primer, it is said that n -factor of 12-14 is recommended for a sailplane, 11-13 for motor glider, 10-12 for a clean wind tunnel, 9 for an average wind tunnel and 4-8 for a dirty WindTunnel [8]. Thus, it is expected that a typical low-speed aircraft operates at a complete range of analysed n -factor between 4 and 12.

2.3.5 User defined transition locations

The following Fig.2.17 shows the various forced transition locations between the leading edge and the free transition location in plot of pressure distribution. Since the free transition occurs at

approximately $x/c = 0.85$, values between 0.1 and 0.8 were chosen for calculations.

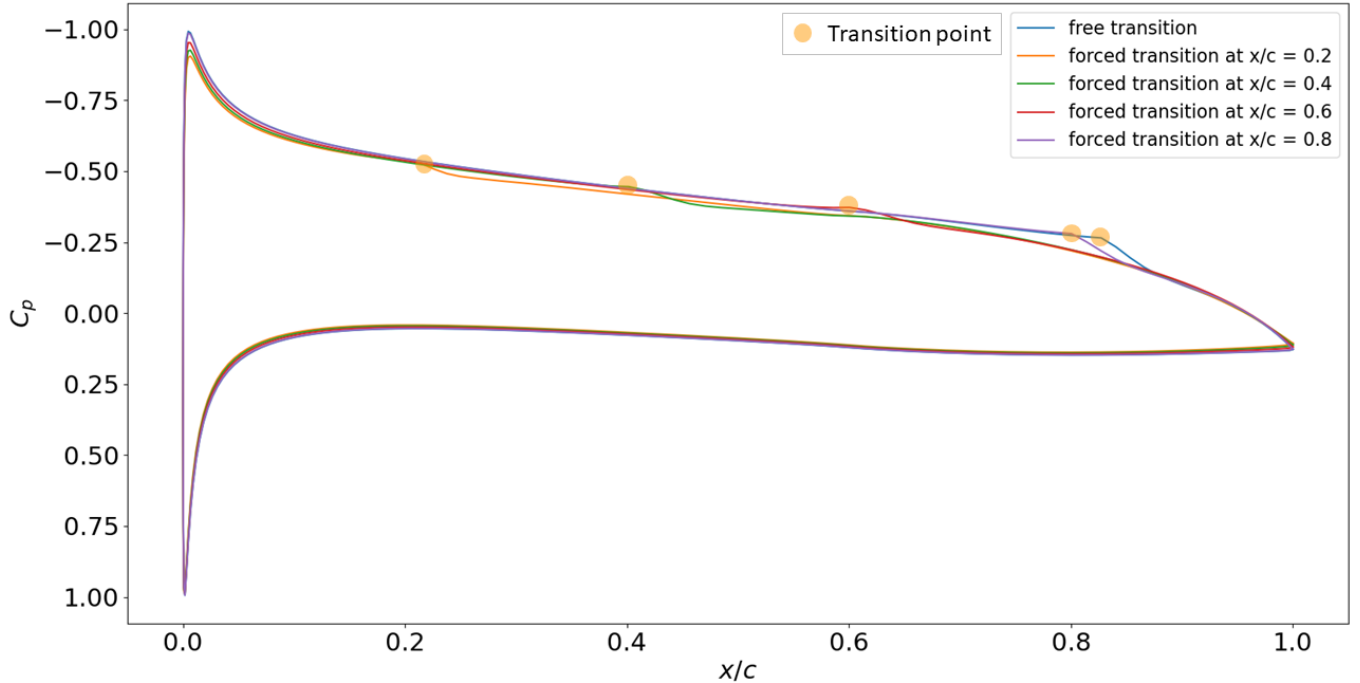


Fig. 2.17 Free and forced transition locations of NACA 2607 at $Re = 5 \times 10^5$, n-factor = 9 and $\alpha = 2^\circ$

It can be seen that as the location of forced transition move towards the leading edge, the laminar separation bubble gets smaller and is almost non-existent near the leading edge (at $x/c = 0.1$).

Table 2.4 Drag coefficients, C_d , at $C_l = 0.5$ for various forced transition locations, x/c , at $Re = 5 \times 10^5$, n-factor = 9 and $\alpha = 2^\circ$

forced at $x/c =$	0.1	0.2	0.3	0.4	0.5	0.6	0.7	0.8	None (natural)
C_d	0.00917	0.00854	0.00794	0.00736	0.00677	0.00618	0.00566	0.00529	0.00524

This data is also visualised in the following Fig.2.18

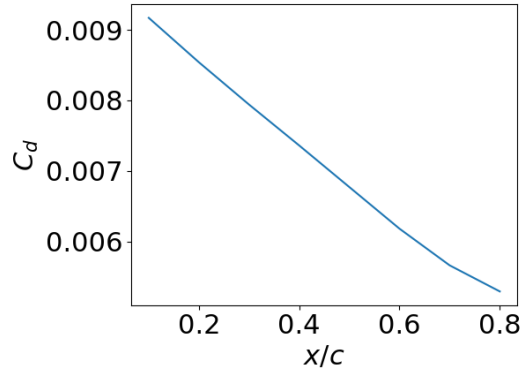


Fig. 2.18 Drag coefficients, C_d , at $C_l = 0.5$ for various forced transition locations, x/c , at $Re = 5 \times 10^5$, n-factor = 9 and $\alpha = 2^\circ$

As the forced transition is moved closer to the leading edge, the drag coefficient, C_d , increases almost linearly as shown in the figure above.

In conclusion, although the laminar separation bubble gets significantly smaller as the forced transition location is moved towards the leading edge, the drag increases. The early transition causes the boundary layer to be majorly formed with a turbulent flow which, in this case, has a more significant increase in drag than the reduction in drag made by the smaller bubble.

2.3.6 Critical roughness height

The "critical roughness height" is the minimum height of surface roughness required to produce forced boundary layer transition [9]. This height is defined in the equation of critical roughness Reynolds number, given by [9] as shown below.

$$Re_{k_k} = \frac{\rho_k u_k k}{\mu_k} \quad (2.8)$$

where k is the roughness height. If Re_{k_k} is smaller than the critical value, no change is made on the location of transition. However, if the value exceeds the critical value, the transition location will be shifted.

3 Assignment 3

3.1 Difference between leading-edge slat and trailing-edge flap

A leading-edge slat is shown in Fig.3.1. When it is deployed, the leading edge extends forward (towards the left in the figure) and downwards. On the other hand, a trailing-edge flap is shown in Fig.3.2. It is deployed simply by rotating downwards. Ultimately, both increases the camber of the airfoil.



Fig. 3.1 Leading-edge slat [10]



Fig. 3.2 Trailing-edge flap [11]

The leading-edge slat allows for a higher value of angle of attack, α , by delaying stall as shown in Fig.3.3 indicated by $\Delta\alpha_{max}$ which is the additional amount of α that can be increased before the stall.

As for the trailing-edge flap, it allows for higher lift coefficient at the same α as shown in Fig.3.3 indicated by ΔC_L which is the amount at which the $C_L - \alpha$ curve has shifted up by.

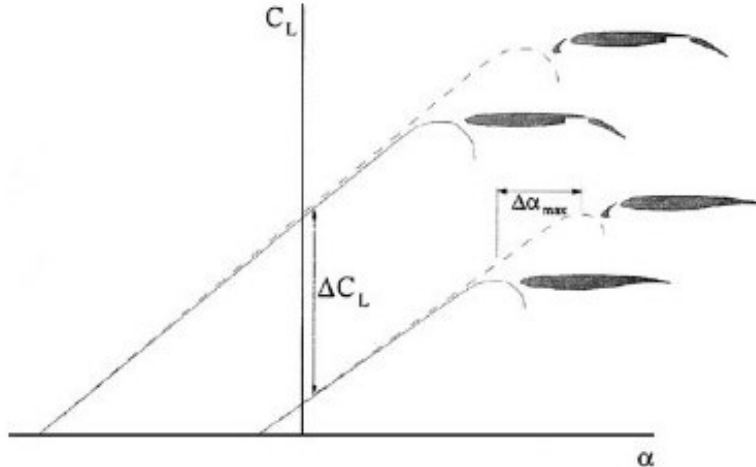


Fig. 3.3 C_L V.s. α of various configurations [12]

Usually, both are deployed during take-off, landing and other low-speed flights but retracted during cruise due to the additional drag they impose on the wings.

3.2 Main effects that determine the behaviour of a high lift system

3.2.1 Slat effect

At a positive angle of attack, the streamlines around a simple isolated airfoil are as shown in Fig.3.4. This results in an adverse pressure peak on the nose of the airfoil to counteract centrifugal forces that are induced by the high-speed flow that wraps around the nose. To reduce this pressure peak, a slat can be introduced.

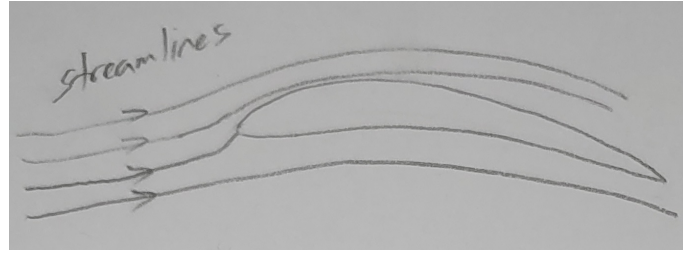


Fig. 3.4 Simple isolated airfoil

The effect of slat can be closely represented using a point vortex as shown in Fig.3.5. It can be seen that the velocities induced by the point vortex at the nose of the airfoil are of opposite direction compared to the streamlines shown in Fig.3.4. Thus, these velocities ultimately reduce the pressure peaks to a large extent. This allows for a delay in the stall angle of attack and a small increase in total lift [13].

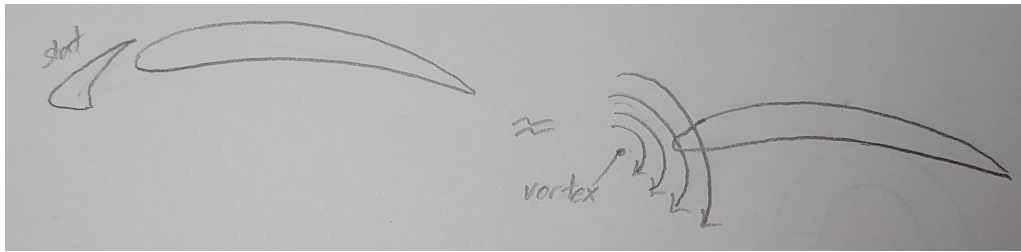


Fig. 3.5 Slat effect

3.2.2 Circulation effect

The circulation effect is used to represent a slotted flap as shown in Fig.3.6. Just like it was done for the slat effect, a point vortex is introduced behind the trailing edge to closely replicate the effect of this slotted flap. This point vortex induces an increase in circulation to a large extent via the introduction of cross-flow (flow which is approximately orthogonal to the streamline) at the trailing edge, thus largely increasing the lift.

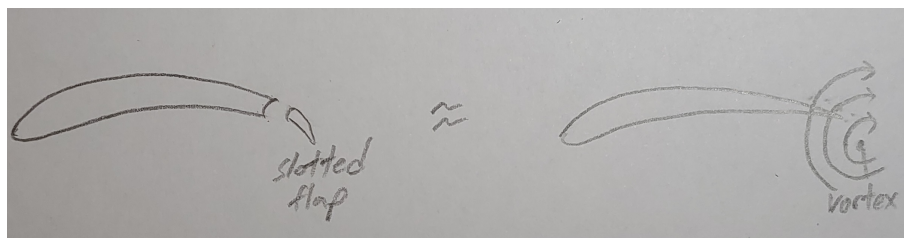


Fig. 3.6 Circulation effect

3.2.3 Dumping effect

The dumping effect follows up from the circulation effect. With the example of the point vortex in Fig.3.6, not only does the cross-flow increases circulation but it also increases the tangential velocities downstream of the trailing edge (or forward element in a case of actual slotted flap). This ultimately results in the boundary layer of the forward element, shown in Fig.3.7, coming off at a higher velocity than the freestream and this helps in the reduction of pressure-recovery demands [13].

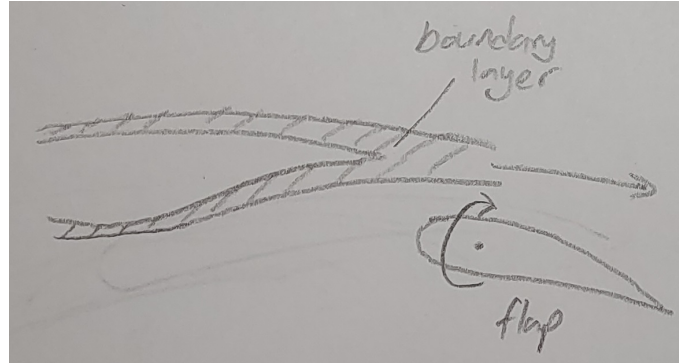


Fig. 3.7 Dumping effect

3.2.4 Off-the-surface pressure recovery

In a single element airfoil, the boundary layer slows down in contact with the airfoil surface to match the required pressure at the trailing edge as shown in Fig.3.8. However, in a multielement airfoil, for example, an airfoil with a leading-edge slat as shown in Fig.3.9, there exists wake that is not in contact with any wall, in a higher pressure region. This wake is formed due to the boundary layer of the slat which comes off the slat at a higher velocity than the freestream velocity. Its recovery (deceleration) back to the freestream velocity off a wall is more efficient than that in contact with the wall.

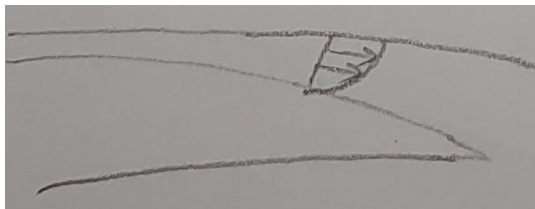


Fig. 3.8 Single element airfoil boundary layer

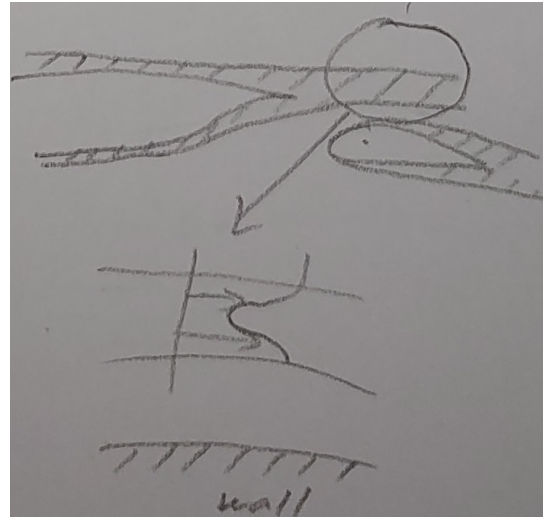


Fig. 3.9 Multielement airfoil boundary layer

3.2.5 Fresh boundary layer effect

Around every element in a multielement airfoil, there is an independent boundary layer that is thinner than that around a single element airfoil as shown in Fig.3.9. Since a thinner boundary layer can sustain greater adverse pressure gradients than a thicker boundary layer, the separate boundary layers of a multielement airfoil are more effective.

3.3 Wake bursting

Wake bursting is a phenomenon that occurs for a multielement airfoil with a large flap angle δ as shown in Fig.3.10.

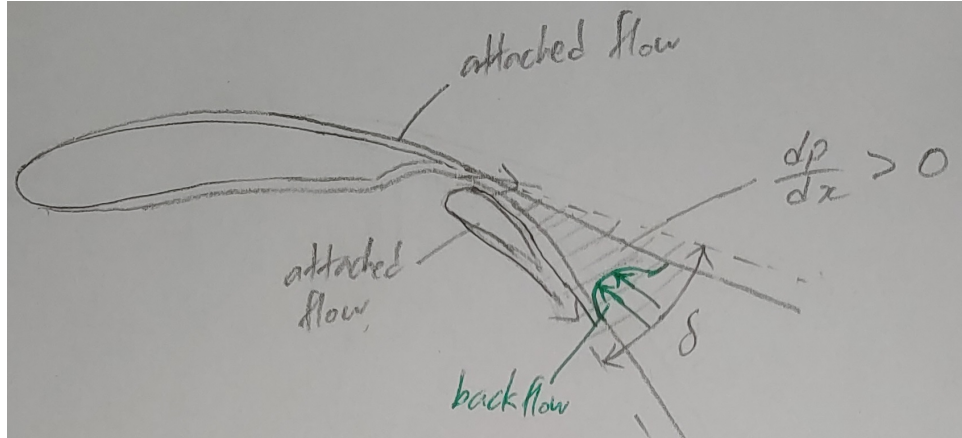


Fig. 3.10 Wake bursting

According to the Kutta condition, the boundary layer of the forward element tends to come off tangential to the trailing edge and the same goes for the rear element. However, due to the large δ , these 2 tangential directions are largely different and an area of positive pressure gradient is formed as shaded in Fig.3.10. This causes the wake of the forward element to grow downstream and incur backflow as shown in green in Fig.3.10. This backflow causes the average flow direction to have a smaller vertical component which leads to a reduction in total lift.

The growth of a wake depends on the Reynolds number of the flow to a large extent. The smaller the Reynolds number, the larger the wake and more off-the-surface pressure recovery which in turn causes greater wake bursting effect [14]. This statement is supported by the experiment presented in [15] done on a multielement airfoil which presents the following Fig.3.11. It shows that the lower Reynolds number leads to a smaller lift which is indeed the effect of wake bursting.

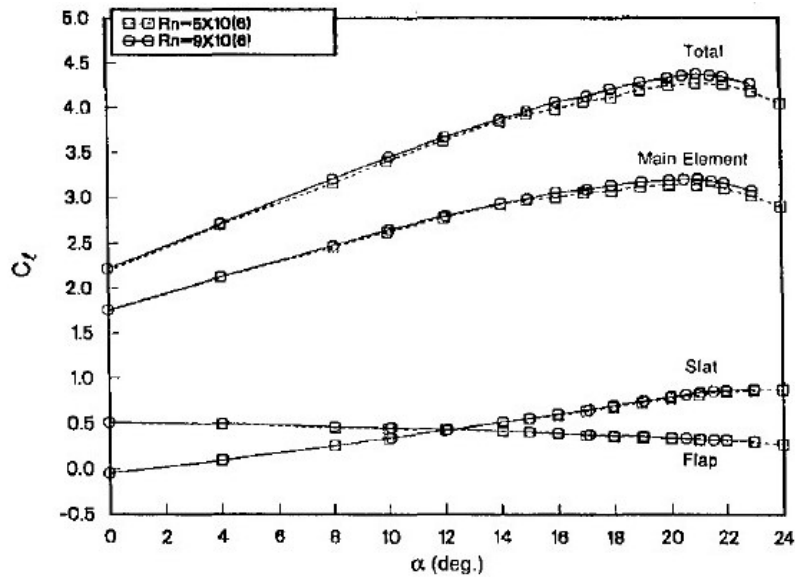


Fig. 3.11 Reynolds Number Effect on Lift, 30P/30N Configuration [15]

It is also said in [15] that the decrease in Reynolds number "increases the wake widths and shifts the wakes farther from the surface of the flap" and "a greater tendency toward off-body recirculation is present at the lower Reynolds number" which supports the aforementioned claim made by [14].

3.4 Relevant 2D-case of GA(W)-1 airfoil

The GA(W)-1 airfoil was used as the relevant case [16]. This multielement airfoil encompasses the Fowler flap. In the reference material, flap settings of 'Nested flap', 10° , 15° , 20° , 25° , 30° and 40° are analysed at Reynolds number of 2.2×10^6 . Thus, these settings, together with the same Reynolds number, will be used and analysed in the assignment. First of all, the airfoil at 'Nested flap' and 20° settings are as shown in Fig.3.12 and Fig.3.13 respectively.

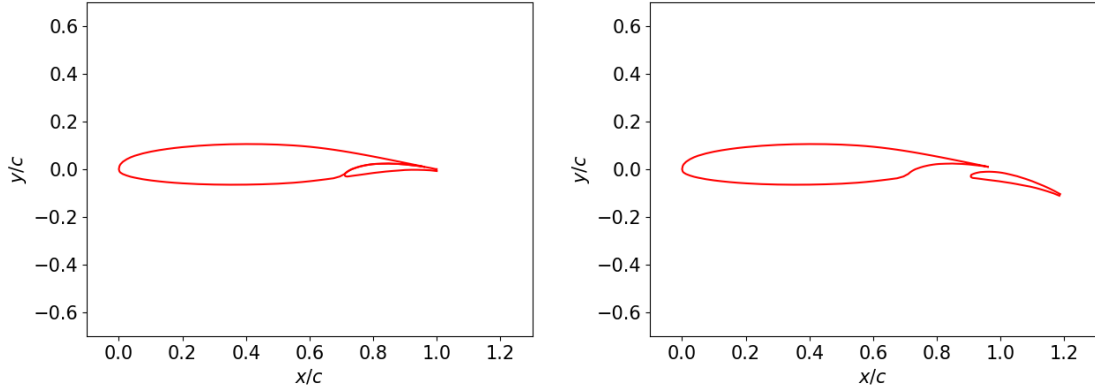


Fig. 3.12 GA(W)-1 with nested flap

Fig. 3.13 GA(W)-1 with flap at 20°

Using JavaFoil [17] with *Eppler standard* transition model and *Calcfoil* stall model, the lift polars of the various settings and the main airfoil without the flap deployed were obtained and plotted together with the experimental data given in [16] as shown from Fig.3.14 till Fig.3.22.

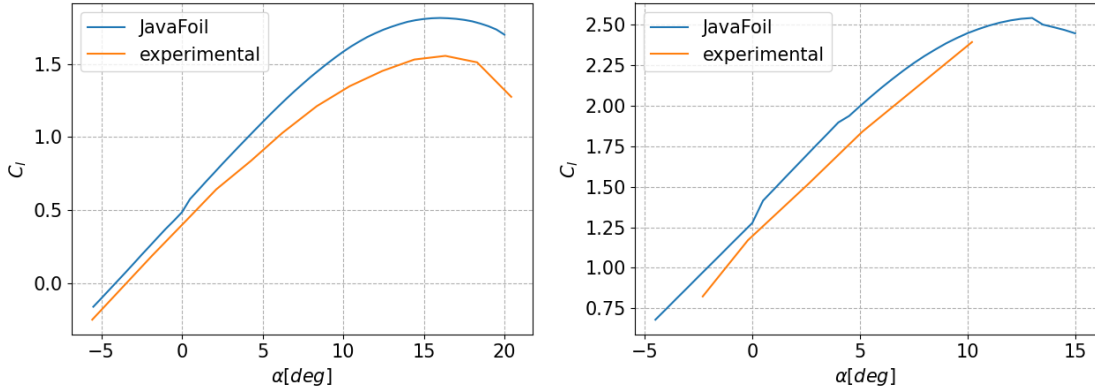


Fig. 3.14 Lift polar of GA(W)-1 with nested flap

Fig. 3.15 Lift polar of GA(W)-1 with flap at 10°

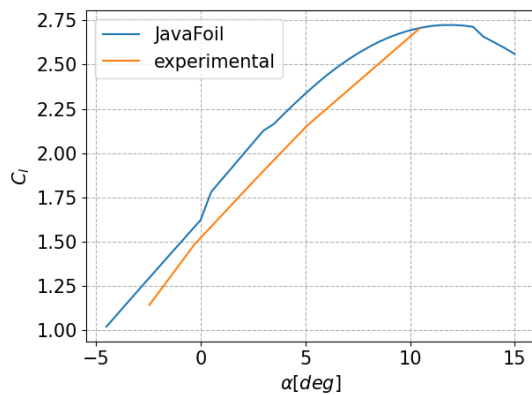


Fig. 3.16 Lift polar of GA(W)-1 with flap at 15°

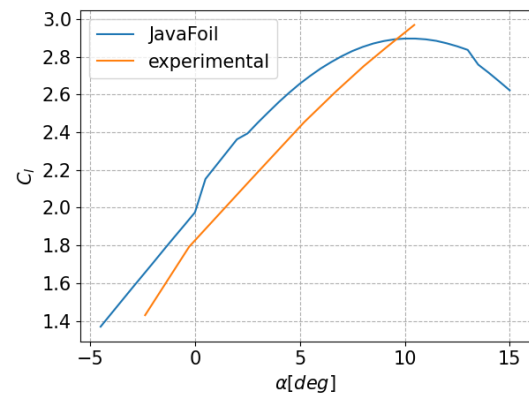


Fig. 3.17 Lift polar of GA(W)-1 with flap at 20°

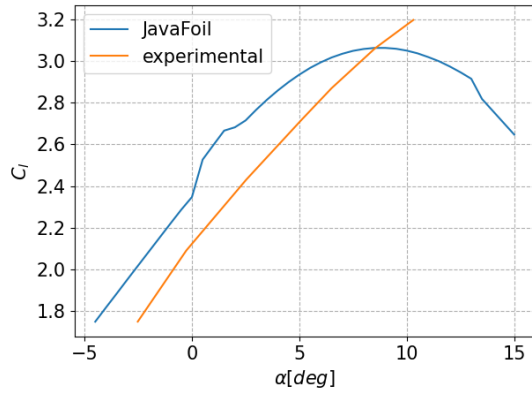


Fig. 3.18 Lift polar of GA(W)-1 with flap at 25°

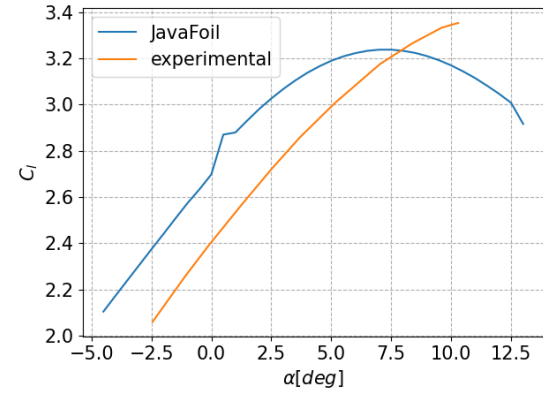


Fig. 3.19 Lift polar of GA(W)-1 with flap at 30°

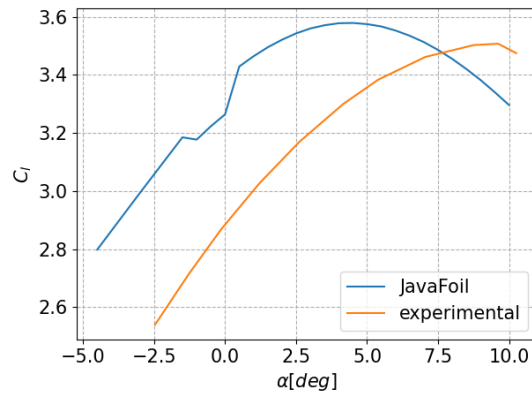


Fig. 3.20 Lift polar of GA(W)-1 with flap at 40°

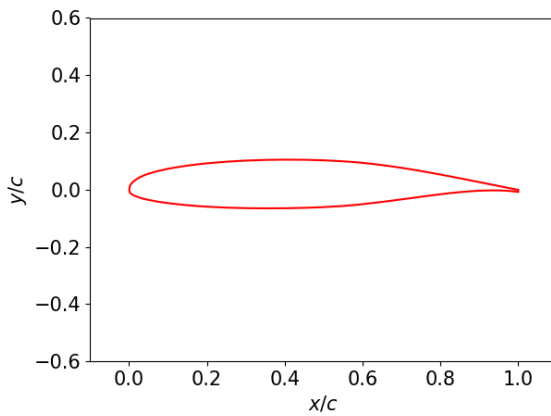


Fig. 3.21 GA(W)-1 without flap

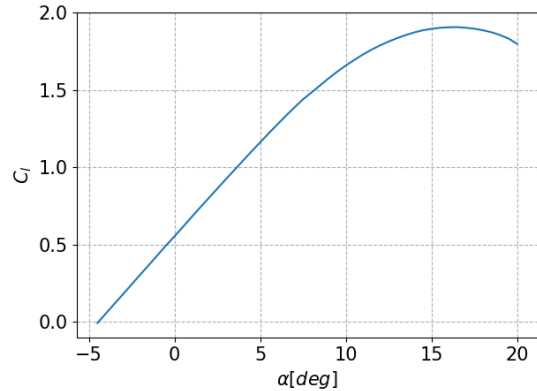


Fig. 3.22 Lift polar of GA(W)-1 without flap

It can be observed that as the angle of the fowler flap increases, the upward shift in slopes of the curves of JavaFoil data from the experimental data increases. This means that the program overestimates the lift. Furthermore, the stall angles of the various settings seem to differ between data of JavaFoil and experimental data as well. JavaFoil utilises a higher-order panel method for the potential flow analysis and integral method for boundary layer analysis [18]. Due to the simplicity of the program, it does not model laminar separation bubbles and turbulent flow separation. Furthermore, it does not take into account the interaction of trailing wakes and the boundary layers of the elements in a multielement airfoil nor the fresh boundary layer effect [18]. Thus, this could be a reason for the overestimation of the lift whereby backflow is neglected and the reduction in the lift is not accounted for.

3.4.1 Pressure field

Using JavaFoil, the pressure fields around GA(W)-1 multielement airfoil at flap settings of 15° ($\alpha = 10^\circ$) and 40° ($\alpha = 5^\circ$) were obtained at Reynold number of 2.2×10^6 . The plots are shown in Fig.3.23 and Fig.3.24.

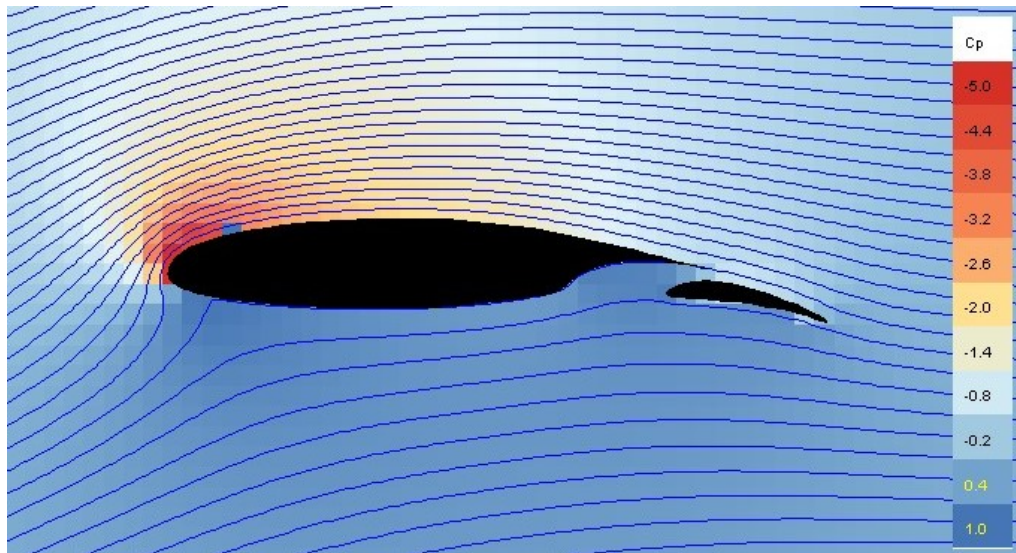


Fig. 3.23 Flowfield around GA(W)-1 with flap at 15° , $\alpha = 10^\circ$, $Re = 2.2 \times 10^6$

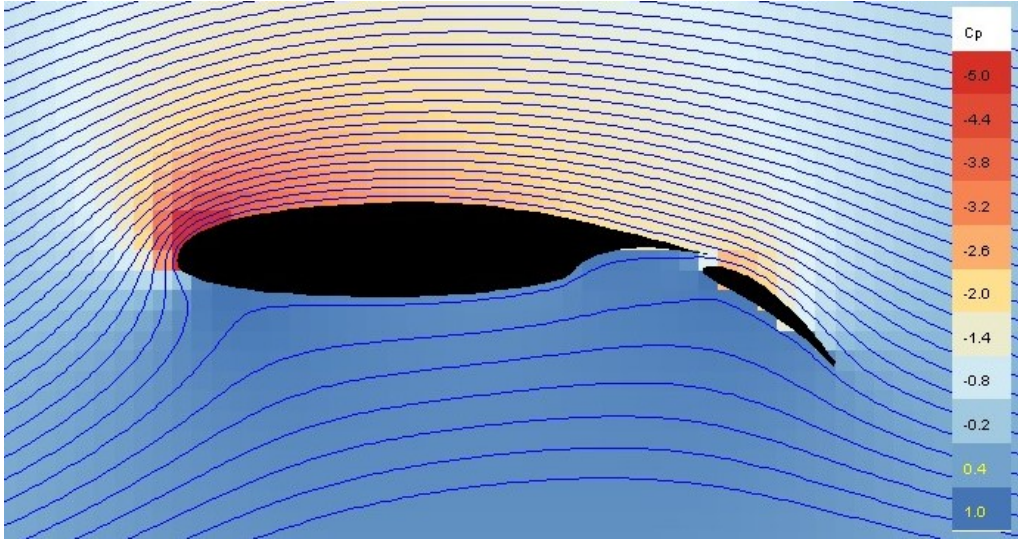


Fig. 3.24 Flowfield around GA(W)-1 with flap at 40° , $\alpha = 5^\circ$, $Re = 2.2 \times 10^6$

The flow field presented in Fig.3.23 meets my expectation to a certain extent. The high pressure at the lower surface and low pressure at the upper surface of the main element are well represented, as well as the high pressure on the lower surface of the flap. However, the streamlines are absent in the cove area which means that the multielement fresh boundary layer effect is not represented.

Similarly, the flow field presented in Fig.3.24 meets my expectation to a small extent. The high pressure at the lower surfaces near leading edges of both the main element and flap is well represented, as well as the low pressure at the upper surfaces. However, the streamlines do not reflect any flow separation nor wake bursting effect at the wake of the main element. Thus, it can be concluded that JavaFoil can analyse multielement airfoil only to a very limited extent.

3.4.2 Plain flap

For the model with plain flap, the main element of GA(W)-1 airfoil has been taken and a plain flap was introduced directly in this airfoil using JavaFoil as shown in Fig.3.25. The flow field is presented in Fig.3.26 and the plots of lift polar and pressure distributions are shown in Fig.3.27 and Fig.3.28 respectively.

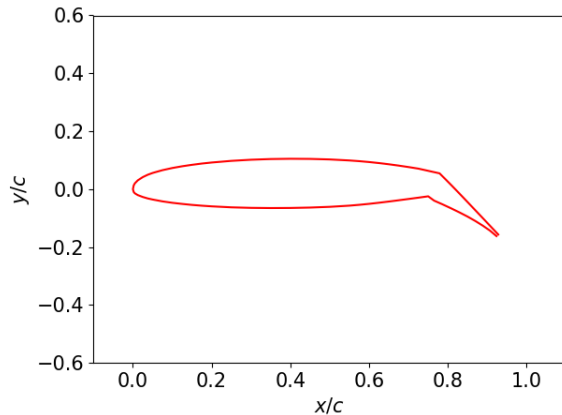


Fig. 3.25 GA(W)-1 airfoil with plain flap at 40°

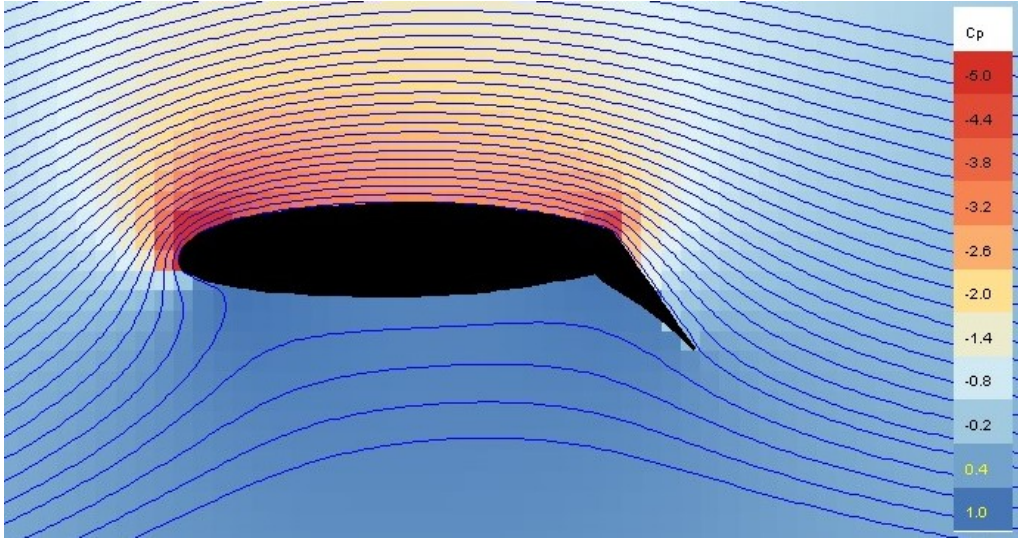


Fig. 3.26 Flowfield around GA(W)-1 with plain flap at 40° , $\alpha = 5^\circ$, $Re = 2.2 \times 10^6$

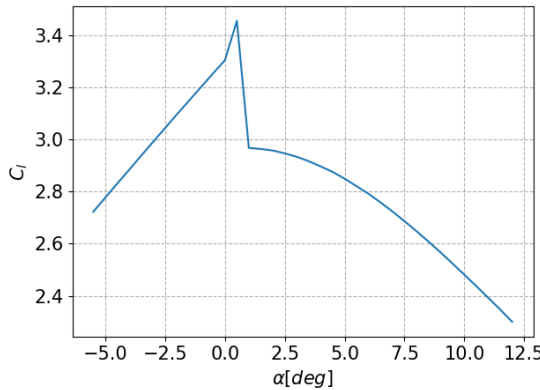


Fig. 3.27 Lift polar of GA(W)-1 with plain flap at 40° , $\alpha = 5^\circ$, $Re = 2.2 \times 10^6$

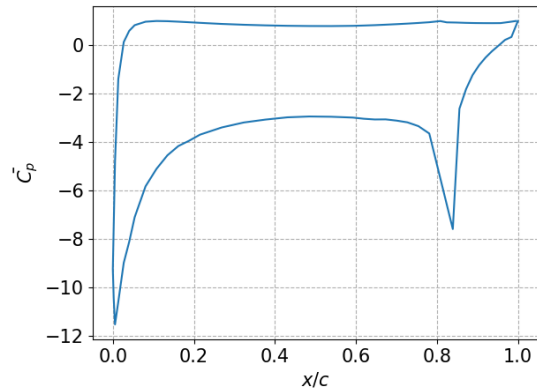


Fig. 3.28 Pressure distribution of GA(W)-1 with plain flap at 40° , $\alpha = 5^\circ$, $Re = 2.2 \times 10^6$

It can be observed from Fig.3.26 and Fig.3.28 that there exist largely negative pressure on the upper surface near leading and trailing edges of the main element. Once again, flow separation is not represented in this flow field which is expected at this setting of high flap angle of 40° .

Additionally, it can be realised that compared to Fig.3.20 which is the lift polar of GA(W)-1 with Fowler flap, the lift polar of GA(W)-1 with plain flap in Fig.3.27 shows similar behaviour for $\alpha \leq 0$ approximately. However, for $\alpha > 0$, there is a clear difference between the two. While the one with Fowler flap maintains the slope only to gradually decrease to eventually run into a stall, the one with plain Flap faces a drastic drop in C_l until about $\alpha \approx 1$ where it further decreases but at a less drastic gradient.

Although this drastic drop in C_l after $\alpha \approx 0$ seems poor compared to the one with Fowler flap when compared to the lift polar of GA(W)-1 without any flap as shown in Fig.3.22, the inclusion of plain flap can generate much more lift at low angles of attack.

3.4.3 Boundary layer effects

The canonical pressure distribution for flap setting of 10° , 20° and 30° for 2 different angles of attack each were plotted as shown from Fig.3.29 till Fig.3.34. The larger of the 2 angles of attack was selected by taking the α close to the stall angle and the other was chosen as a value approximately in the middle of 0° and the stall angle.

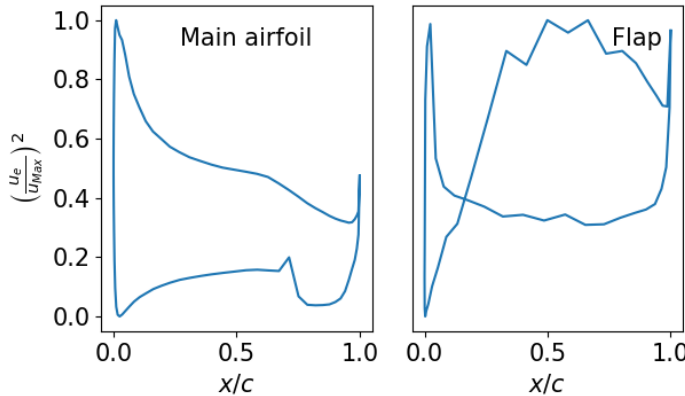


Fig. 3.29 Pressure distribution of GA(W)-1 with flap at 10° , $\alpha = 5^\circ$, $Re = 2.2 \times 10^6$

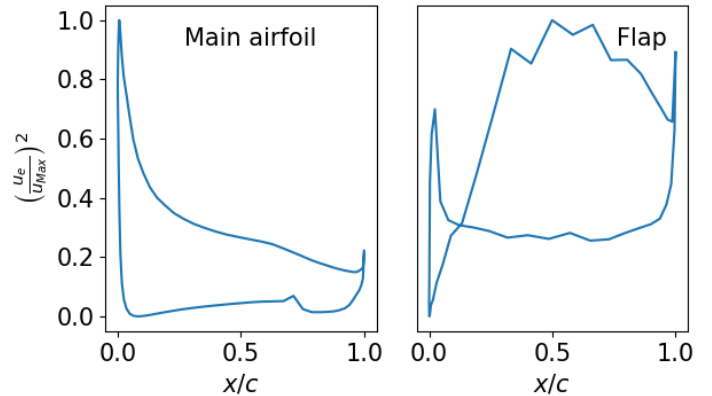


Fig. 3.30 Pressure distribution of GA(W)-1 with flap at 10° , $\alpha = 12^\circ$, $Re = 2.2 \times 10^6$

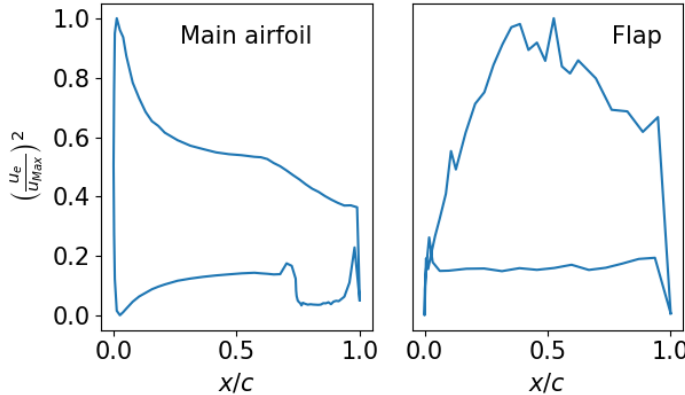


Fig. 3.31 Pressure distribution of GA(W)-1 with flap at 20° , $\alpha = 2^\circ$, $Re = 2.2 \times 10^6$

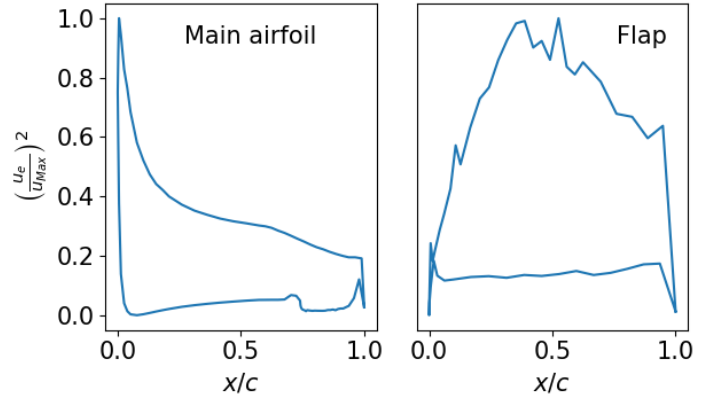


Fig. 3.32 Pressure distribution of GA(W)-1 with flap at 20° , $\alpha = 8^\circ$, $Re = 2.2 \times 10^6$

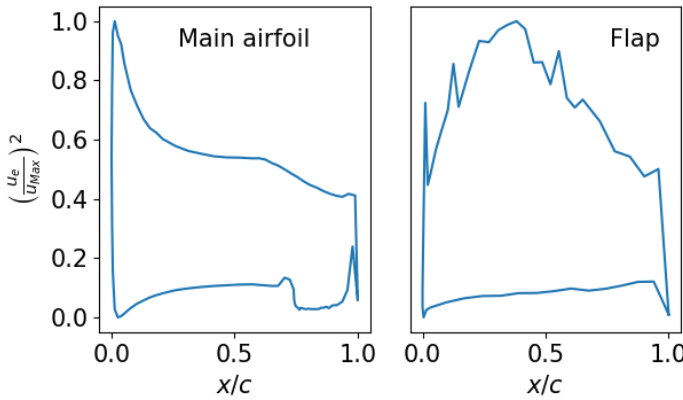


Fig. 3.33 Pressure distribution of GA(W)-1 with flap at 30° , $\alpha = 0^\circ$, $Re = 2.2 \times 10^6$

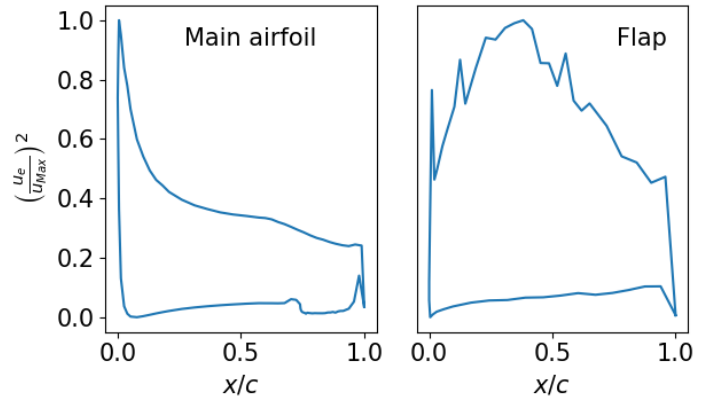


Fig. 3.34 Pressure distribution of GA(W)-1 with flap at 30° , $\alpha = 5^\circ$, $Re = 2.2 \times 10^6$

Wake bursting effect of these set of pairs (flap setting and α) were then analysed using Gartshore's approximate relation. It is said that if (3.1) holds, so if the left-hand side is larger than the right-hand side, the wake grows and otherwise, the wake decays.

$$\frac{1}{1 - \bar{C}_p} \cdot \frac{d\bar{C}_P}{dx} > \frac{0.007}{\delta^*} \quad (3.1)$$

Both the left and the right hand sides of (3.1) were plotted as shown from Fig.3.35 till Fig.3.46.

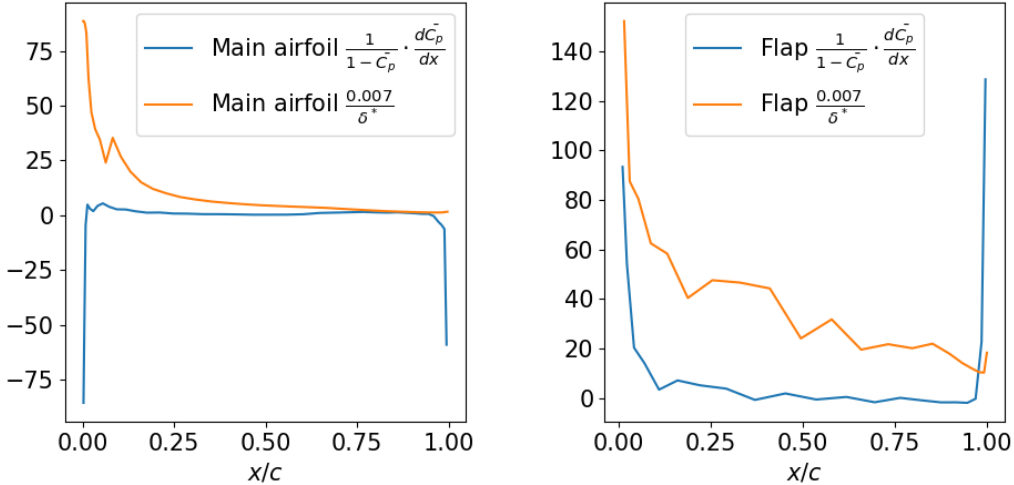


Fig. 3.35 Gartshore relation analysis of GA(W)-1 with flap at 10° , $\alpha = 5^\circ$

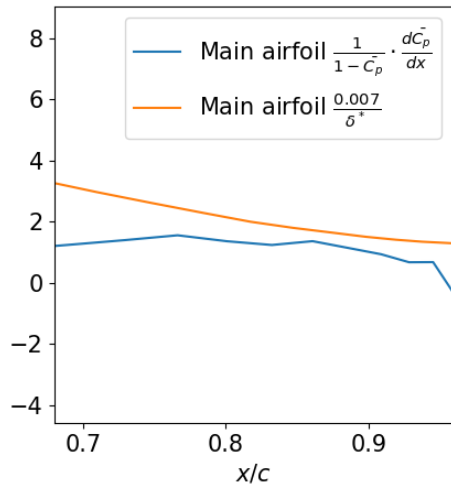


Fig. 3.36 Zoomed-in Fig. 3.35 (left plot: main airfoil)

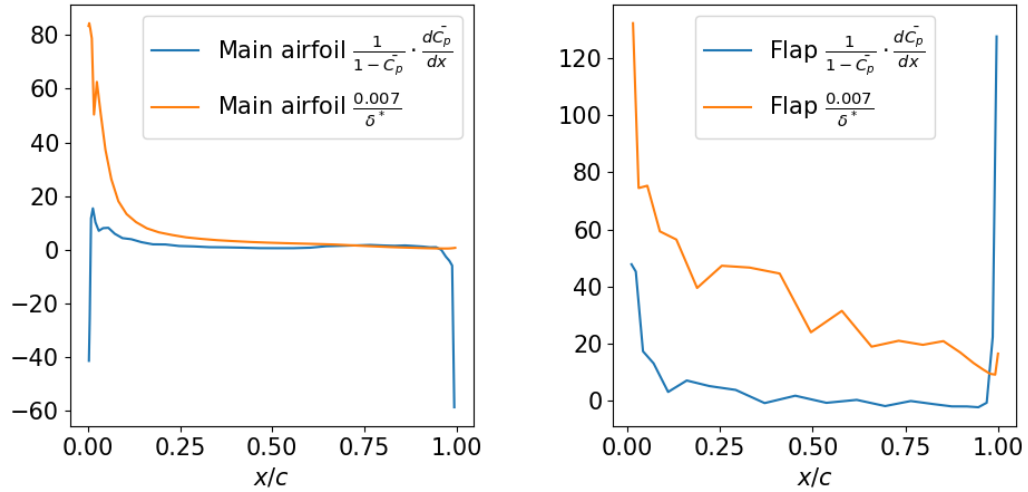


Fig. 3.37 Gartshore relation analysis of GA(W)-1 with flap at 10° , $\alpha = 12^\circ$

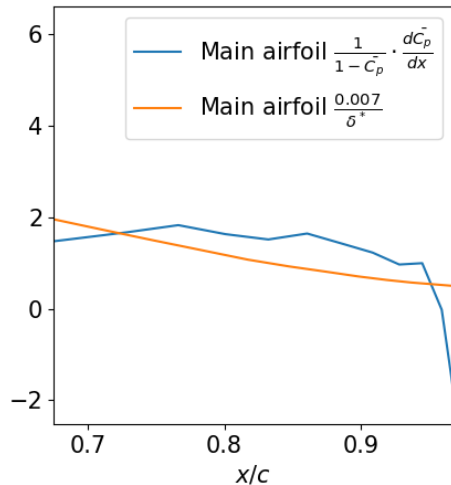


Fig. 3.38 Zoomed-in Fig. 3.37 (left plot: main airfoil)

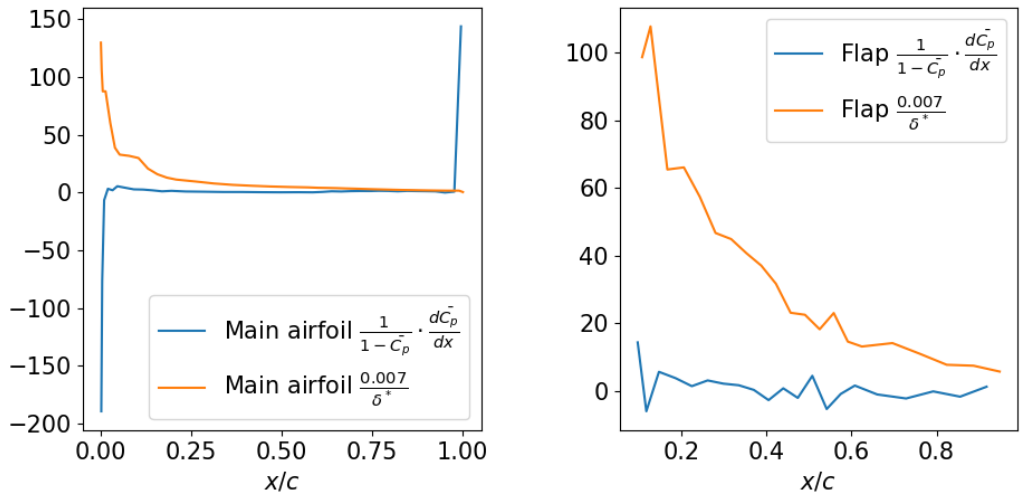


Fig. 3.39 Gartshore relation analysis of GA(W)-1 with flap at 20° , $\alpha = 2^\circ$

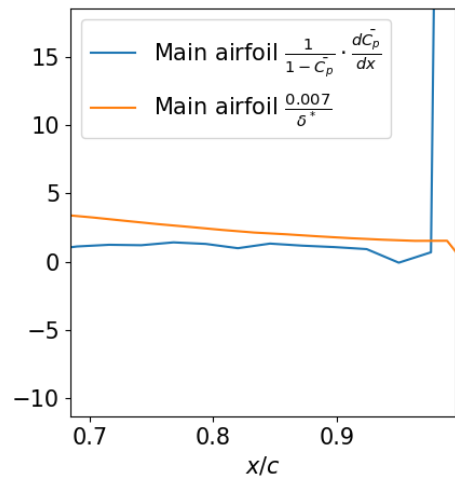


Fig. 3.40 Zoomed-in Fig. 3.39 (left plot: main airfoil)

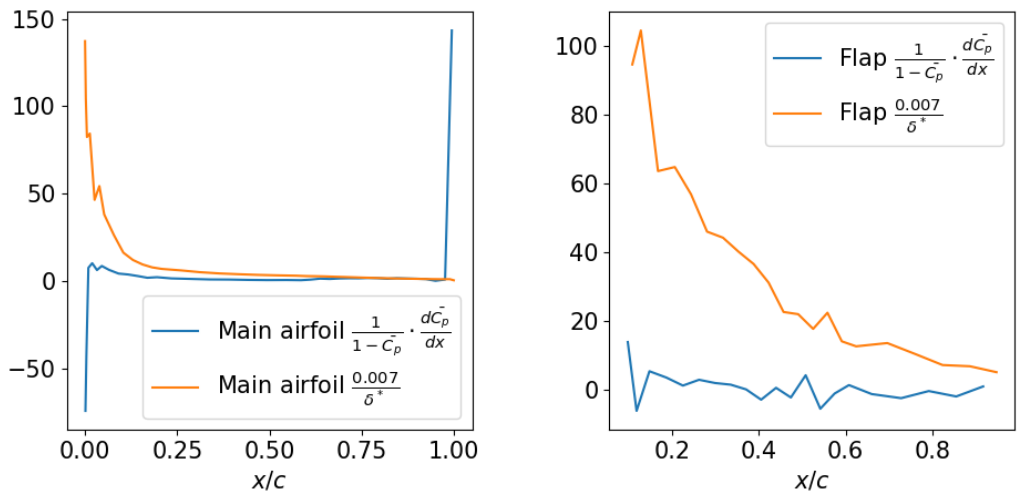


Fig. 3.41 Gartshore relation analysis of GA(W)-1 with flap at 20° , $\alpha = 8^\circ$

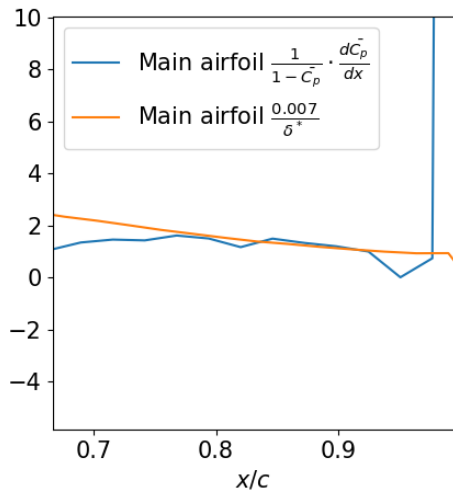


Fig. 3.42 Zoomed-in Fig. 3.41 (left plot: main airfoil)

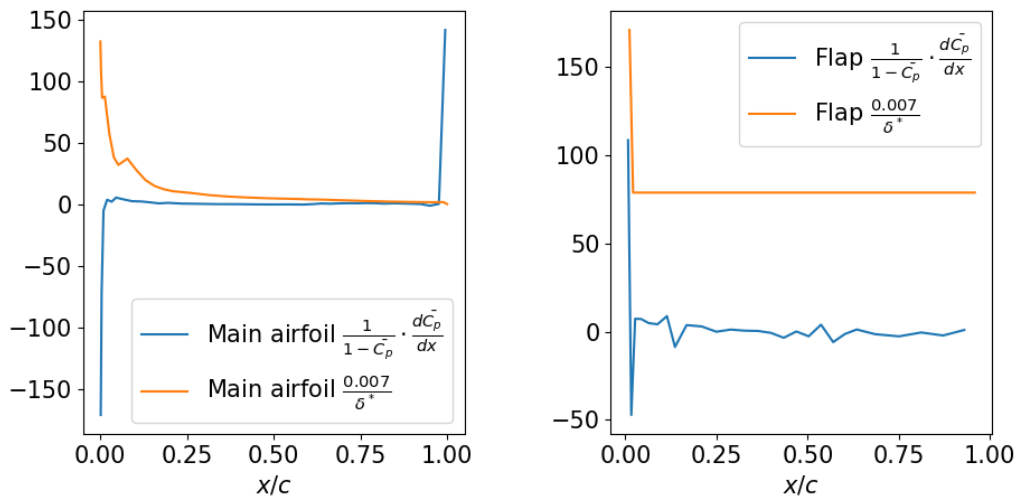


Fig. 3.43 Gartshore relation analysis of GA(W)-1 with flap at 30° , $\alpha = 0^\circ$

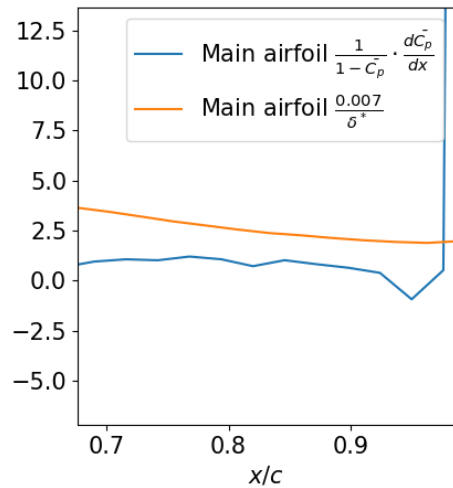


Fig. 3.44 Zoomed-in Fig. 3.43 (left plot: main airfoil)

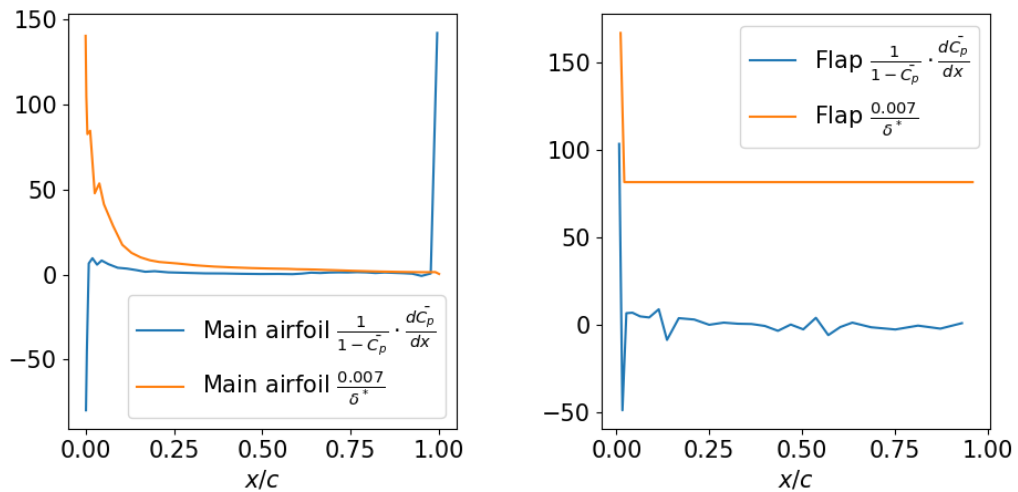


Fig. 3.45 Gartshore relation analysis of GA(W)-1 with flap at 30° , $\alpha = 5^\circ$

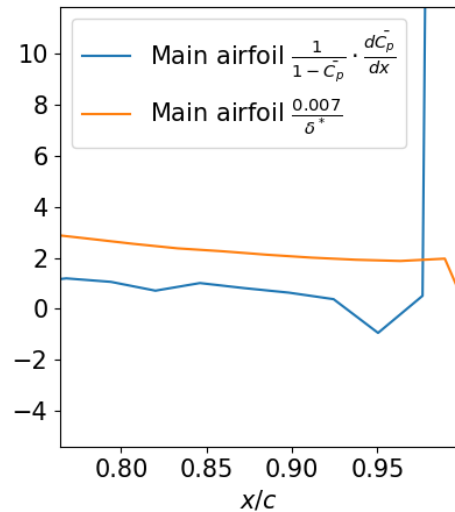


Fig. 3.46 Zoomed-in Fig.3.45
(left plot: main airfoil)

The results shown in above plots are discussed in Table 3.1 below.

Table 3.1 Discussion of wake growth and decay

Flap setting	alpha	main airfoil	Flap
10°	5°	Wake decays throughout	Wake decays until about $x/c = 0.9$ where wake starts to grow
	12° (stall)	Wake decays until about $x/c = 0.72$ where wake starts to grow and it decays again near trailing edge	Wake decays until about $x/c = 0.9$ where wake starts to grow
20°	2°	Wake decays until the trailing edge where wake starts to grow	Wake decays throughout
	8° (stall)	Wake decays until about $x/c = 0.83$ where wake grows for a short moment and decays again. However, wake starts growing again near trailing edge	Wake decays throughout
30°	0°	Wake decays until trailing edge where wake starts to grow	Wake decays throughout
	5° (stall)	Wake decays until trailing edge where wake starts to grow	Wake decays throughout

It can be concluded from Table 3.1 that the GA(W)-1 airfoil is prone to wake bursting effect only to a small extent.

4 Assignment 4

4.1 Task 1

4.1.1 Relation between normalwash velocity and dihedral angle

The following equation describes the relationship between normalwash velocity, V_n , and the dihedral angle, θ .

$$V_n = k \cdot \cos(\theta) \quad (4.1)$$

where k is a constant. This relation applies to every discretized element of the wing in which various values of dihedral angle, θ , can exist and not just for the winglet. At a certain value of the dihedral angle, a specific value of normalwash velocity is produced due to the wingtip vortices. For example, for a basic horizontal wing ($\theta = 0^\circ$) without any winglet, downward normalwash (downwash) of $V_n = k$ is experienced through the entire span of the wing. This idea can be extended to wings with winglets as shown in Fig.4.1 and Fig.4.2 whereby two different and extreme configurations of winglets at a dihedral angle of $\theta = 90^\circ$ and 0° are presented respectively.

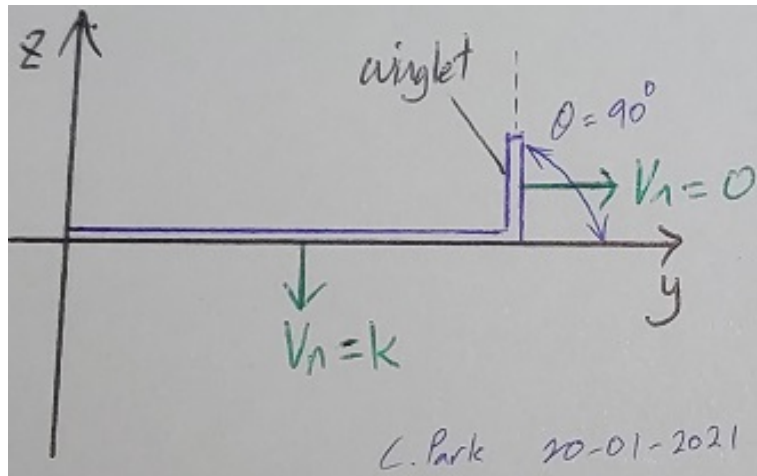


Fig. 4.1 Optimal normalwash, V_n , for $\theta_{winglet} = 90^\circ$

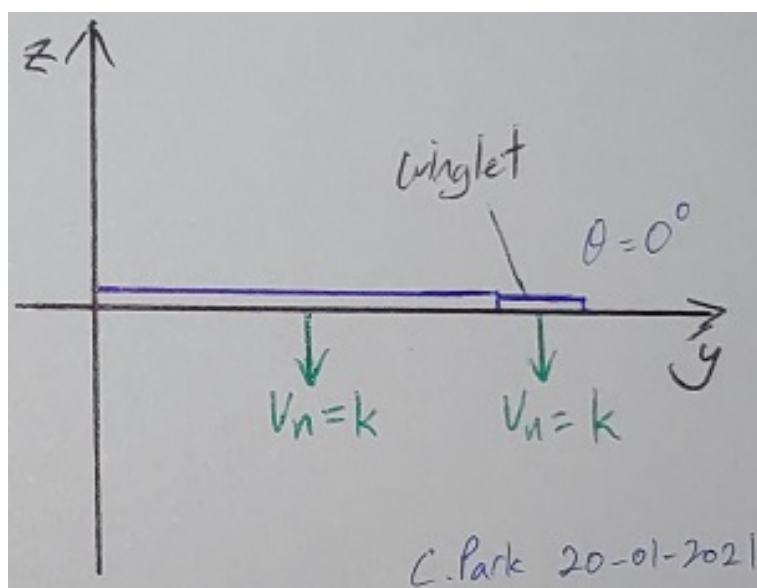


Fig. 4.2 Optimal normalwash, V_n , for $\theta_{winglet} = 0^\circ$

Fig.4.1 presents a horizontal wing with the winglet at $\theta = 90^\circ$. According to (4.1), this implies that the normalwash (outward sidewash) is 0. On the other hand, Fig.4.2 presents a horizontal wing with winglet which is also horizontal, at $\theta = 0^\circ$, making the entire wing planar. This gives a normalwash of k according to (4.1) which agrees with the claim made by Munk in 1921 that the downwash in the wake behind the ideally loaded planar wing is constant [19].

It can thus be observed that any realistic dihedral angle of winglet between 0° and 90° have normalwash which consists of both vertical and horizontal components. These components of normal wash are important in determining the effective angle of attack for both the vertical and horizontal tailplanes. Thus, determining the magnitude of V_n can aid in how the aerodynamic performance is altered at the tailplanes.

4.1.2 Reason behind increase in aerodynamic performance with addition of winglets

The total drag of an aircraft can be said to be consisting of the profile drag, induced drag and wave drag. While induced drag is caused by the effects of potential flow, the profile drag is caused by the effects of viscous flow. Although the wave drag is also an effect of viscous flow, the winglets do little to nothing in elevating it and thus will not be discussed further.

Starting with the induced drag, the induced drag is proportional to the inverse of the aspect ratio of the wing and is a three-dimensional potential flow effect which arises due to the tip vortices of the wings. Thus, longer wings have a lower induced drag compared to shorter and broader wings. With the inclusion of winglets, not only are the vortices moved further away from the main wing, the strength of the vortices is significantly reduced thus allowing the potential flow throughout the wings to be more two-dimensional and ultimately reducing the magnitude of the induced drag.

On the other hand, this inclusion of winglets increases the profile drag instead. Since profile drag is due to frictional resistance, the viscous flow plays a part in it. The addition of the winglets adds an amount of wetted area to the total surface of the wing, there is now a greater frictional resistance on the wing and thus a greater profile drag.

However, the magnitude of the reduction in induced drag is much larger than the magnitude of increase in profile drag in general. Furthermore, since the induced drag contributes to almost 50% of the drag during cruise conditions and 80-90% during takeoff according to [20], in overall, the winglets reduces the total drag of the aircraft and thus increase its aerodynamic performance.

4.2 Task 2

The given flight conditions that will be used for the subsequent analyses in the report are: Mach number, $M = 0.7$, Altitude, $h = 7000m$ and Lift coefficient, $C_L = 0.6$. The given altitude results in air density of $\rho = 0.6601kg/m^3$ and gravity of $g = 9.788m/s^2$ [21].

4.2.1 Initial plain wing

Using the given wing planform with root chord of 5.5 m and its leading edge (LE) coordinate of $x, y, z = (0, 0, 0)$, tip chord of 2.0 m and its LE coordinate of $(3.5, 14, 0)$, the analysis on the plain wing was done using the Athena Vortex Lattice (AVL) program and the following is the induced drag of the plain wing obtained from Trefftz plane.

$$C_{D_i} = 0.015457$$

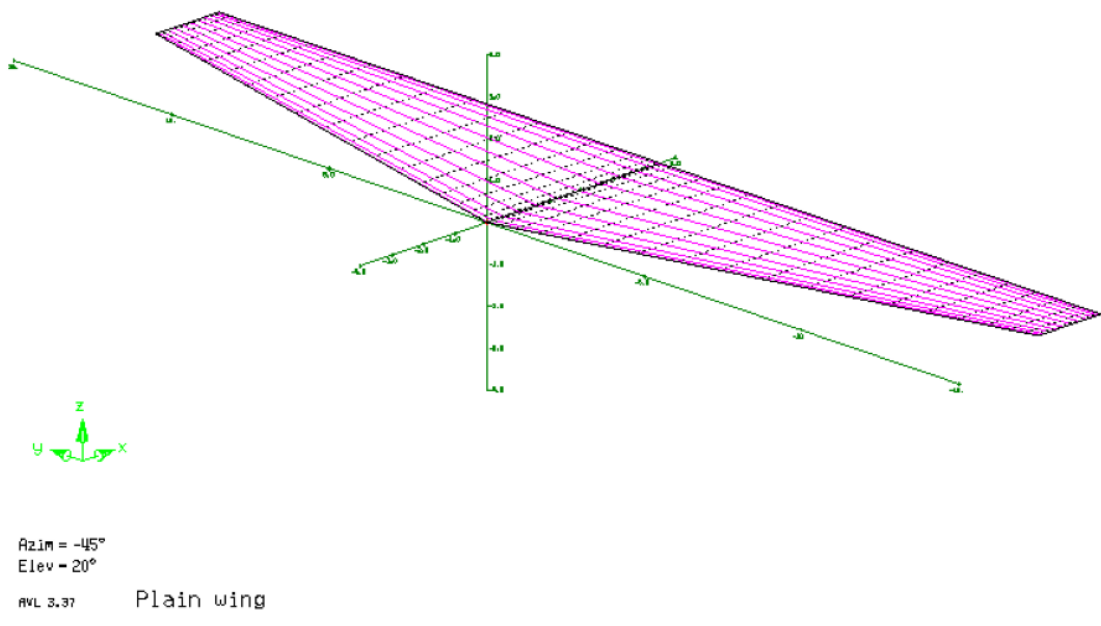


Fig. 4.3 Plain wing configuration

4.2.2 Inclusion of winglet

A winglet was then added to the wing using the provided dimensions as shown in Fig.4.4 with cant angle of 45° as an example.

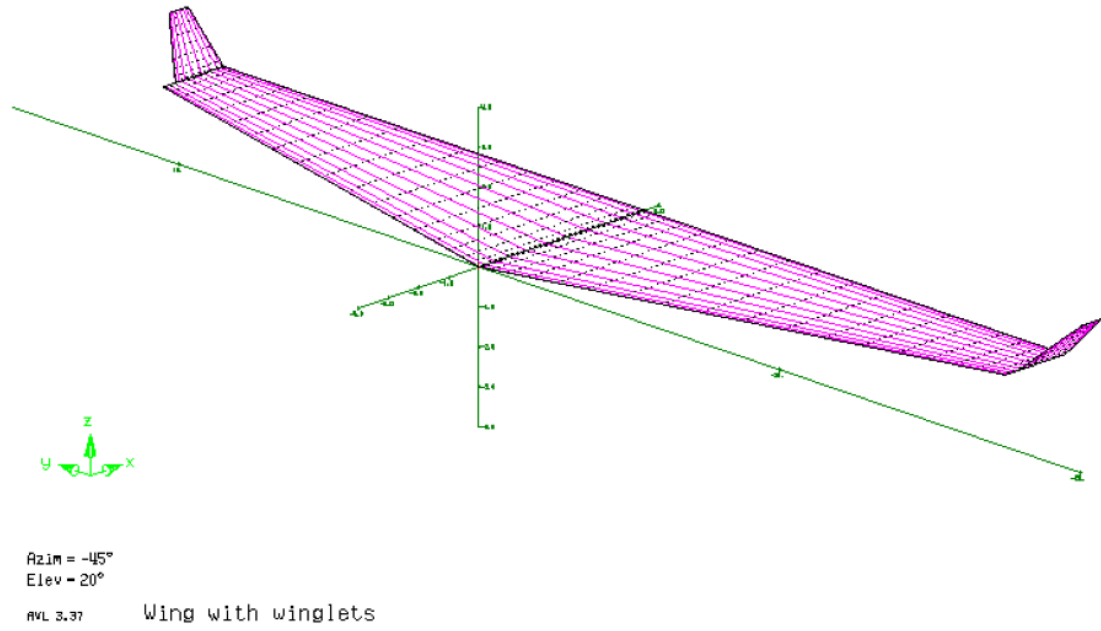


Fig. 4.4 Wing with winglet at $\phi = 45^\circ$

4.2.3 Variance of cant angle

The cant angle was then varied from 0° to 90° with 5° spacing and the induced drag were obtained for each point. These data were then plotted as shown in Fig.4.5 in which the minimum value is indicated by the red dot. This minimum induced drag point represents cant angle of $\phi = 90^\circ$. It can be observed that the induced drag starts converging at around $\phi = 60^\circ$ and although not extended, the curve seems to have completed converging at the indicated minimum point.

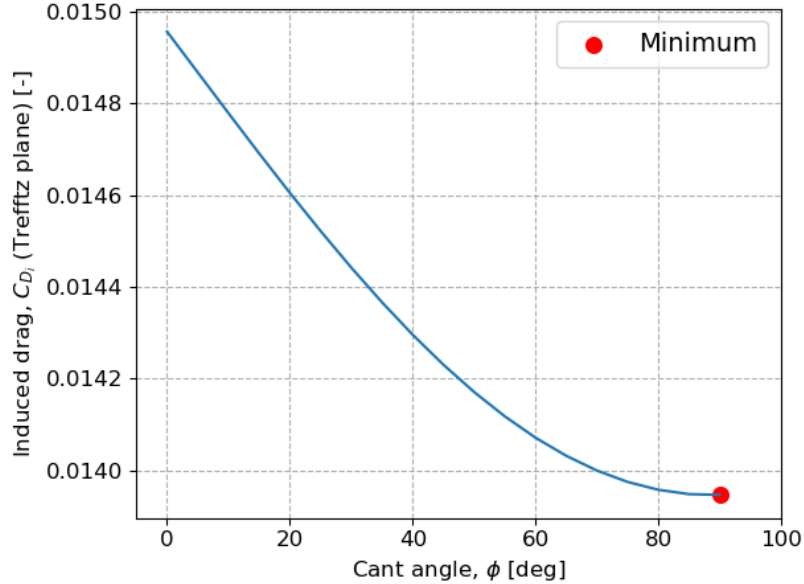


Fig. 4.5 Induced drag, C_{D_i} , against cant angle, ϕ

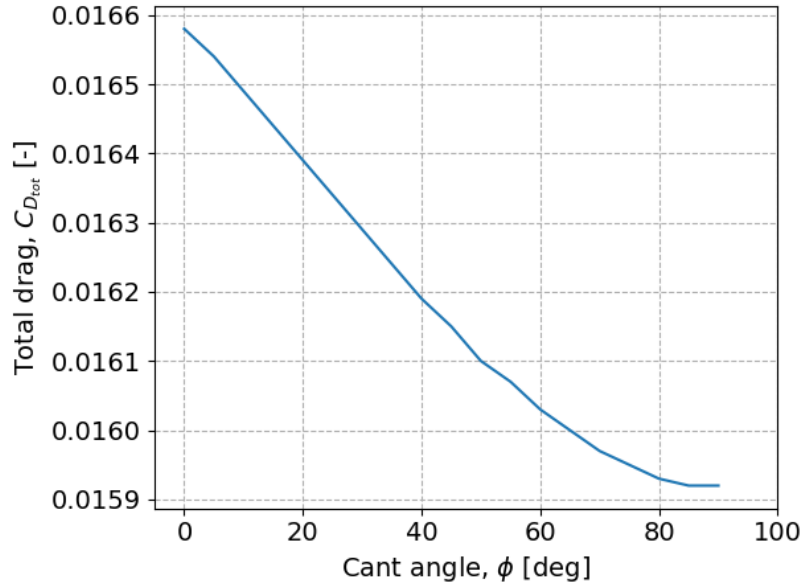


Fig. 4.6 Total drag, $C_{D_{tot}}$, against cant angle, ϕ

Additionally, the total drag was also plotted against the cant angle as shown in Fig.4.6 to show that the minimum induced drag point is not only significant in terms of induced drag but also

the total drag. Thus, it can be realised that cant angle of $\phi = 90^\circ$ is the best design regarding aerodynamic performance.

4.2.4 Variance of verticle winglet height

The cant angle is now fixed at $\phi = 0^\circ$ which makes the winglet purely vertical. The winglet height is to be varied in a sufficiently realistic range. Initially, at $\phi = 0^\circ$, the winglet height equalled to the given length l_w , which is 6% of the wingspan and this has a value of $1.68m$. The induced drag of each of the winglet height was then recorded and plotted as shown in Fig.4.7 in which the red dot represents the initial winglet height and its corresponding induced drag.

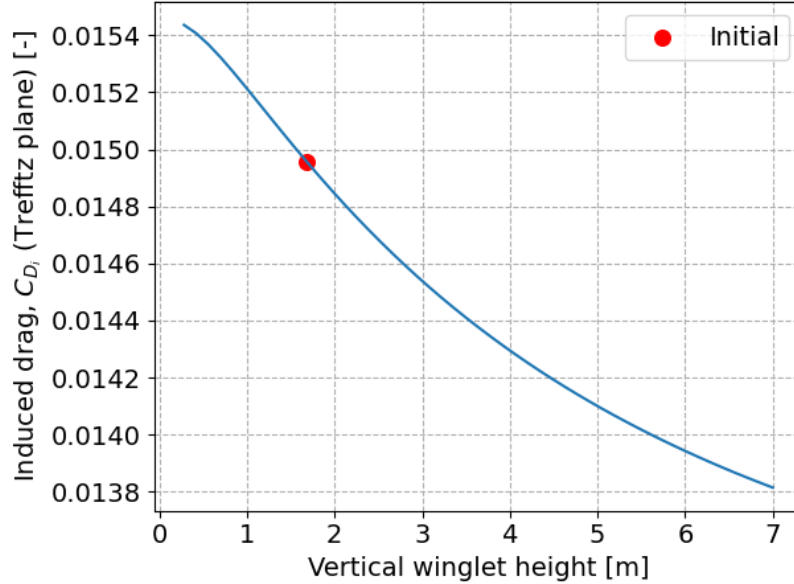


Fig. 4.7 Induced drag, C_{D_i} , against winglet height

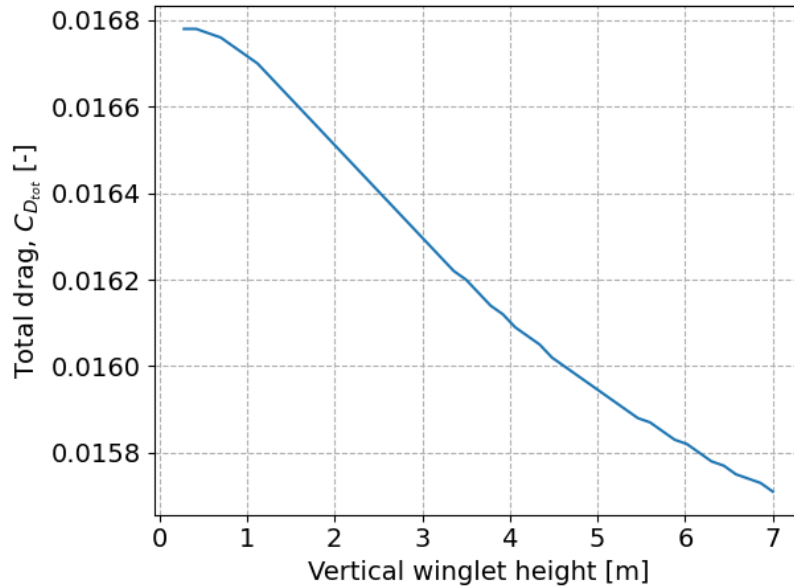


Fig. 4.8 Total drag, $C_{D_{tot}}$, against winglet height

It can be observed from Fig.4.7 that the induced drag, C_{D_i} , decreases almost linearly with the increase in vertical winglet height in the first (left) half of the plot and shows some degree of curvature towards the right. Additionally, it could be confirmed that the reduction in induced drag significantly influences the total drag with total drag displaying similar behaviour with respect to winglet height as shown in Fig.4.8.

In comparison with the simple span extension which is represented by the red dot in Fig.4.5 (since $\phi = 90^\circ$ means that the winglet is in plane with the wing), it can be realised that more than thrice the initial winglet height is required to reach a similar magnitude of induced drag. Although a closer analysis is not done, a simple span extension is a more viable option than tripling the height of the vertical winglet as many critical forces and moments will follow with such a large vertical extension, especially on the joints of the aircraft.

4.3 Task 3

In order to analyse the effect of a winglet on the structural weight of the wing, the root bending moment was calculated. This is since it is said that the root bending moment can be assumed proportional to the wing structural weight.

$$\begin{aligned} S &= \int_0^{b/2} C_l c q dy \\ M &= \int_0^{b/2} S(y) dy \end{aligned} \quad (4.2)$$

Since the winglet was defined as a separate surface in this report, the computation required solving the given integrals for shear force and bending moment as shown in (4.2) using the lift distribution on both the wing and the winglet. The following Fig.4.9 presents the results when the cant angle was varied.

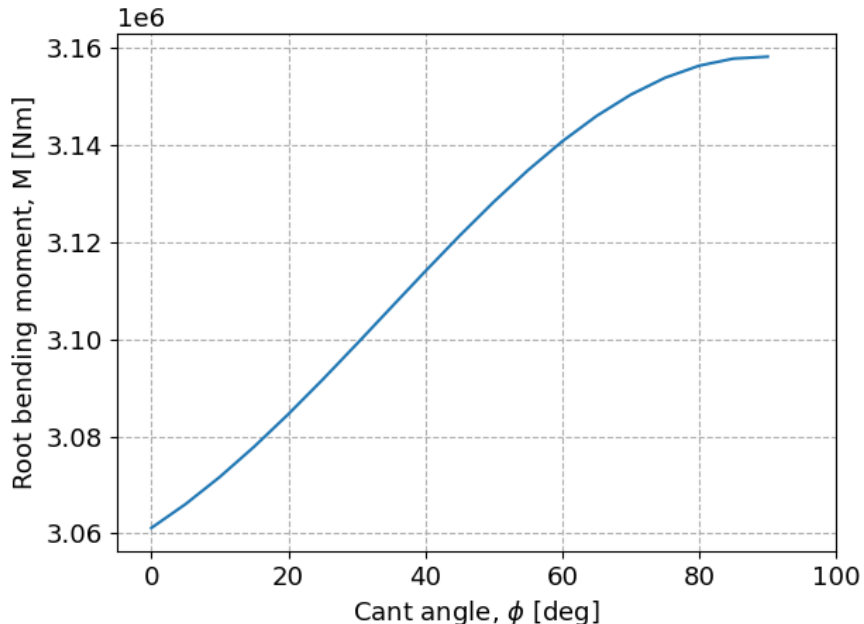


Fig. 4.9 Root bending moment, M , against cant angle, ϕ

It can be observed that the root bending moment has almost a linear increase from $\phi = 0^\circ$ until 60° approximately and afterwards, the curve seems to converge nearly at $\phi = 90^\circ$. Thus, it is

assumed that further increase in cant angle above $\phi = 90^\circ$, so with winglet below horizontal, the bending moment will not increase further. In conclusion, a vertical winglet at $\phi = 0^\circ$ seems to be the best option when the bending moment is of top concern for the aircraft.

4.4 Task 4

Using the given equation as shown in (4.3), the seven winglet design parameters were varies to minimise J for the 3 different values of k .

$$J = k \frac{C_{D_i}}{C_{D_{i_0}}} + (1 - k) \frac{M_r}{M_{r_0}} \quad (4.3)$$

The optimisation was performed using Python's Scipy optimize library [22] which has the *minimize* function. Variable J in (4.3) was then minimised while varying the 7 parameters in the given range as shown in (4.4) for the 3 different values of k , 0, 0.5 and 1.0. The results are then presented in Table 4.1. It was realised that the optimal configuration given for $k = 0$ resulted in the lowest J value as it seen in Table 4.1.

$$\begin{aligned} 0.02b &\leq l_w \leq 0.10b \\ 10^\circ &\leq \phi_w \leq 90^\circ \\ 0.4C_t &\leq C_{w_r} \leq 1.0C_t \\ 0.4 &\leq \lambda_w \leq 1.0 \\ 0^\circ &\leq \Lambda_w \leq 45^\circ \\ \epsilon_{w_r} &\geq -6^\circ; \epsilon_{w_t} \leq 6^\circ \end{aligned} \quad (4.4)$$

Table 4.1 Optimised winglet configuration for $k = 0, 0.5$ and 1.0

k	J	l_w/b	$\phi[\text{deg}]$	C_{w_r}/C_t	λ_w	$\Lambda_w[\text{deg}]$	$\epsilon_{w_r}[\text{deg}]$	$\epsilon_{w_t}[\text{deg}]$	Figure
0.0	1.00070	0.0200548	10.0412	0.992822	0.999994	44.7023	11.9989	5.99902	Fig.4.10
0.5	0.95382	0.0999926	89.7424	0.465119	0.401006	0.113867	-5.90867	4.80183	Fig.4.11
1.0	0.82957	0.0999992	87.4937	0.994772	0.491914	0.0981458	-5.94809	-11.3799	Fig.4.12

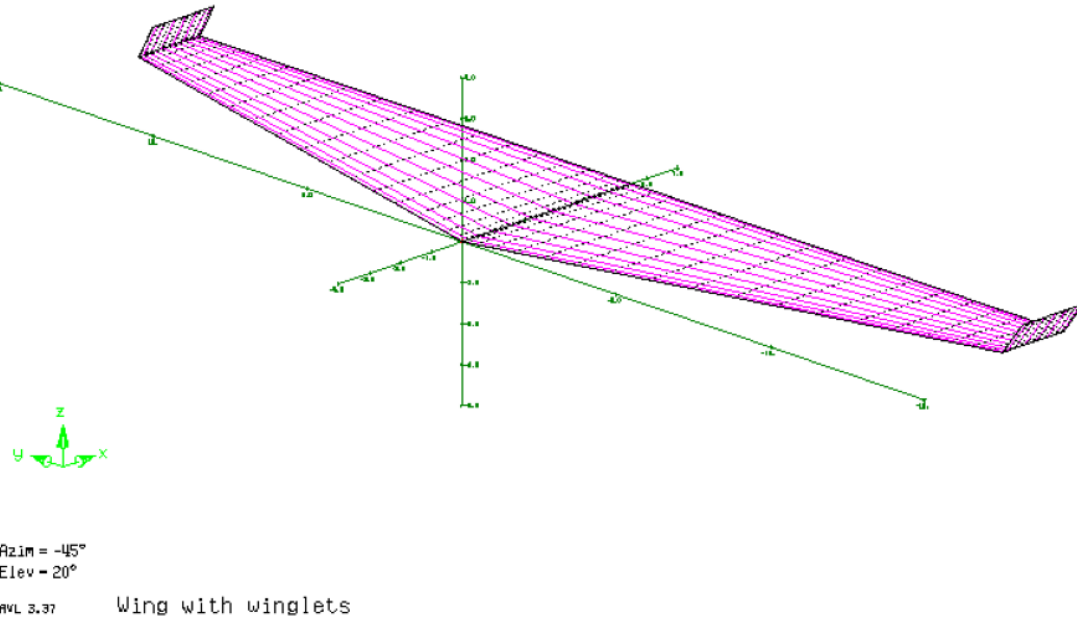


Fig. 4.10 Wing-winglet configuration for $k = 0.0$

For the optimised wing-winglet configuration for $k = 0.0$ as shown in Fig.4.10, it can be seen that the winglets are almost vertical with $\phi \approx 10^\circ$. According to (4.1), this leads to a considerably small magnitude of normalwash thus a small root bending moment is expected. The length of the winglet which is directly related to the moment arm is significantly small compared to the other configurations with $l_w/b \approx 0.02$ which minimises the root bending moment even further but this short length allows the wingtip vortices to still affect the main wing to a large extent. Furthermore, the root and tip chords of the winglet are nearly the same length as the tip chord of the wing. This leads to wingtip vortices that are of similar size as that of the plain wing. Hence, a large induced drag is expected.

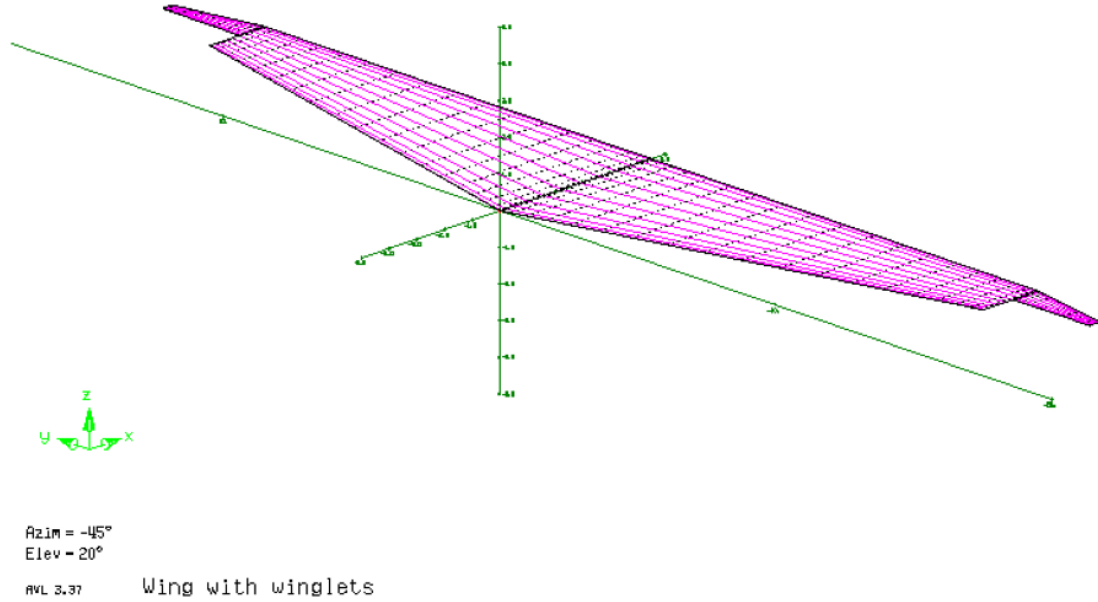


Fig. 4.11 Wing-winglet configuration for $k = 0.5$

Now for the optimised wing-winglet configuration for $k = 0.5$ as shown in Fig.4.11, the winglets are nearly in plane with the main wing body at $\phi \approx 90^\circ$. This implies that the largest possible normalwash is induced according to (4.1). This is worsened by the long winglet of which the ratio to the wingspan is $l_w/b \approx 0.1$ thus resulting in large moment arm. However, due to the small surface area of the winglets, the magnitude of root bending moment is minimised. This small surface from its thin physical appearance leads to small wingtip vortices that allow for small induced drag. Additionally, since the length of the winglet is large, these vortices are placed far away from the main body of the wing. Thus, the induced drag is expected to be small.

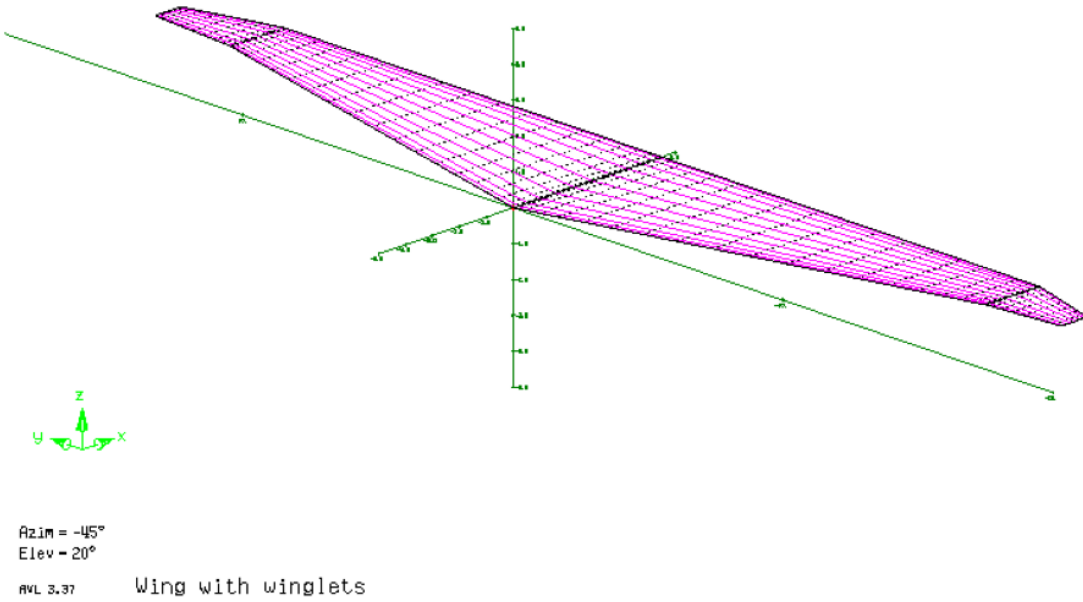


Fig. 4.12 Wing-winglet configuration for $k = 1.0$

Lastly, for the optimised wing-winglet configuration for $k = 1.0$ that is shown in Fig.4.12, the winglets are also almost in plane with the main wing body at $\phi \approx 87^\circ$. Again, according to (4.1), the normal wash is expected to be large. Together with the large length of the winglets that contributes to the moment arm and a significantly larger surface area compared to the configuration of $k = 0.5$, the root bending moment is expected to be much larger as well. Although this configuration features winglets with much larger surface area compared to that of $k = 0.5$, since the winglets are still long and have a slightly smaller cant angle, the value of induced drag is hard to expect in comparison to the induced drag of $k = 0.5$ configuration. However, it can be expected that the induced drag stays small as the tip chord of the winglet is still considerably small and is placed far away from the main wing body.

These claims and expectations are then checked in terms of induced drag and root bending moment using a plot of $C_{D_i}/C_{D_{i_0}}$ against M_r/M_{r_0} that was produced as shown in Fig.4.13.

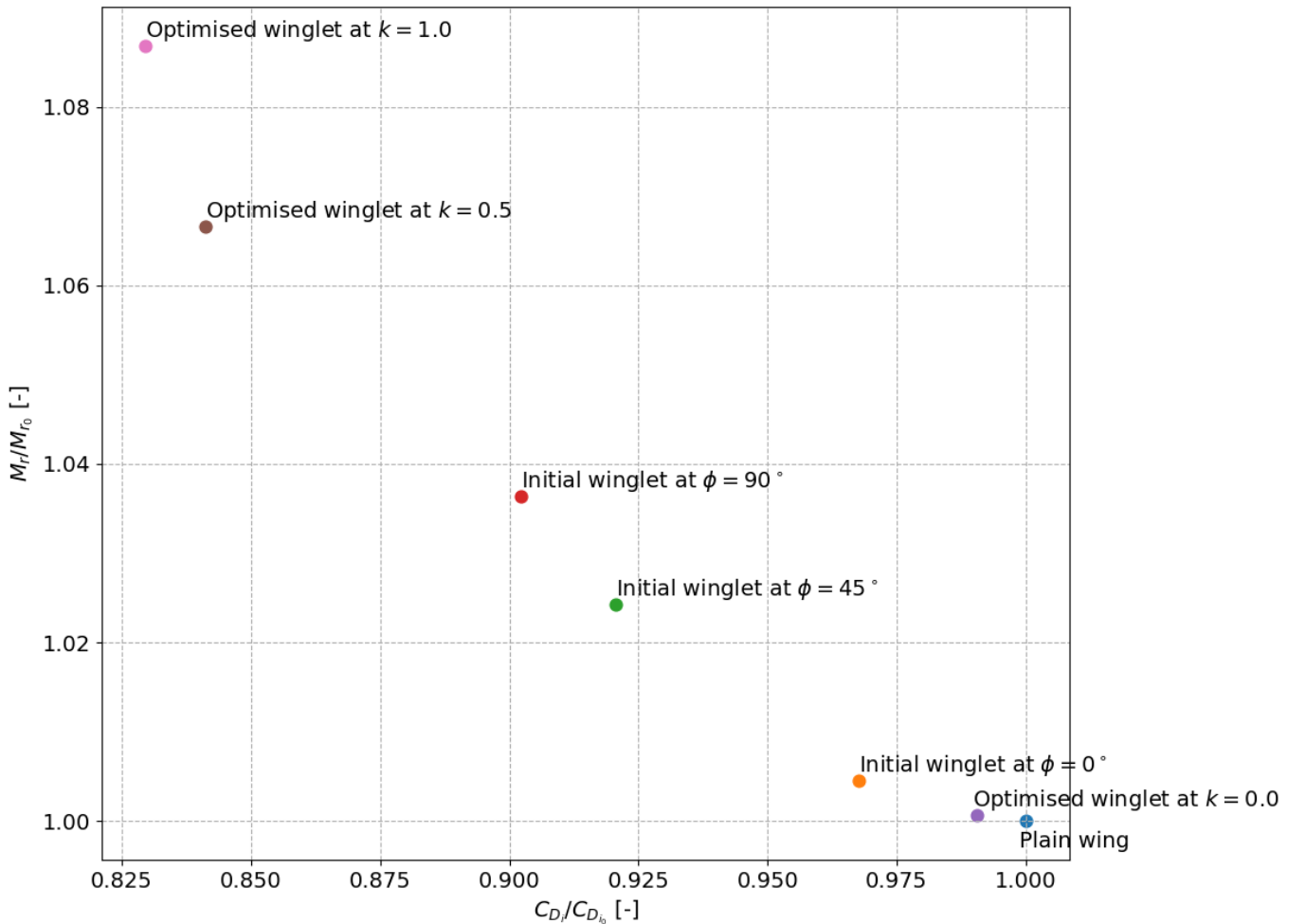


Fig. 4.13 Comparison between various configurations

It can be observed from the data points that the induced drag and root bending moment are almost a trade-off to one another which means that to reduce induced drag, a rise in root bending moment has to be bore. Furthermore, the plot showed almost exactly the expected results for the optimised wing-winglet configurations for $k = 0, 0.5$ and 1.0 . It was ultimately realised that the configuration for $k = 1.0$ has a small induced drag compared to the configuration for $k = 0.5$ which was not so clear from the physical data of Table 4.1.

The optimised winglet for k value of 0.5 seems to be the best configuration due to the large reduction in induced drag compared to the other configurations. Although the configuration for optimised winglet for $k = 1.0$ has a lower induced drag, the price to pay in terms of increase in root bending moment is much larger. Thus, the configuration shown in Fig.4.11 is the best one in my opinion.

In conclusion, I prefer the optimised configuration for $k = 0.5$ as featured in Fig.4.11 and it has the following induced drag and root bending moment:

$$\begin{aligned} C_{D_i} &= 0.013001 \\ M_{root} &= 3.25 \times 10^6 \text{ Nm} \end{aligned} \tag{4.5}$$

5 Assignment 5

5.1 Part 1: The solver

5.1.1 Velocity diagram

The following Fig.5.1 describes the velocity diagram of a propeller blade section at radial position r for a Cartesian coordinate system which consists of tangential t and axial a axes and for a flow accelerating case.

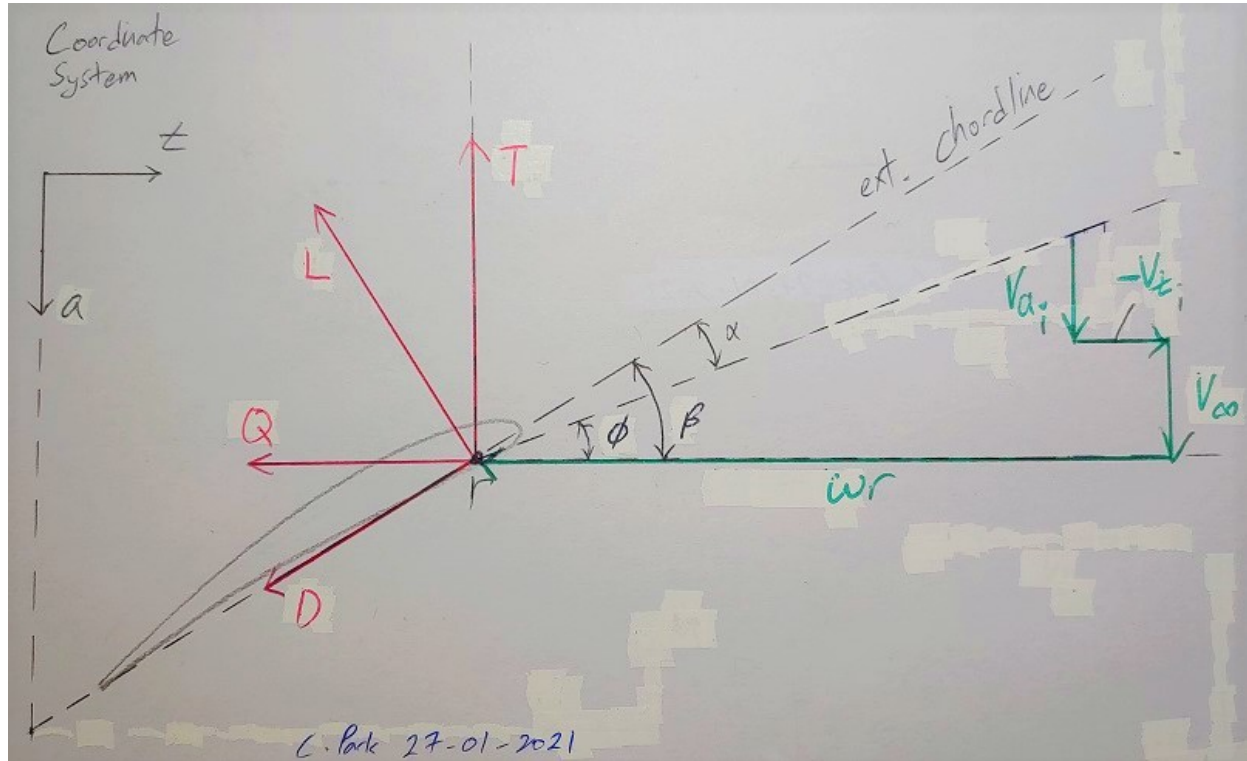


Fig. 5.1 Velocity diagram for a propeller blade section

The parameters presented in the Fig.5.1 represents:

- T : Thrust
- L : Lift
- Q : Torque
- D : Drag
- ϕ : Inflow angle
- β : Pitch angle
- α : Angle of attack
- ω : Angular velocity of propeller rotor
- r : radial location along the propeller blade
- V_∞ : Freestream velocity
- V_{t_i} : Tangential induced velocity ($V_{t_i} < 0$)
- V_{a_i} : Axial induced velocity

5.1.2 Radial distribution of axial and tangential flow velocity

Typical radial distributions of the axial and tangential flow produced by a propeller in flow accelerating case are presented in Fig.5.2.

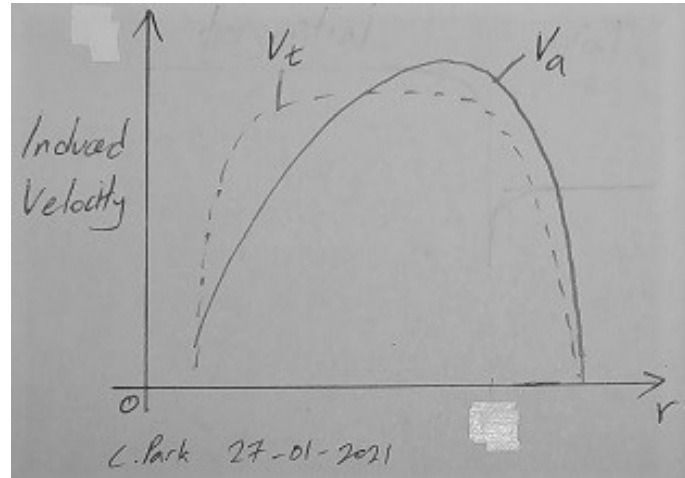


Fig. 5.2 Induced velocity distribution

Firstly for the axial flow velocity, v_a , it starts at an almost 0 value near the root of the propeller blade, so at the hub of the propeller. It then quickly rises to a maximum value near the tip of the propeller blade after which the magnitude falls to 0 drastically.

On the other hand, for the tangential flow velocity, v_t , it also starts at a near 0 value after which it drastically increases at a gradient greater than that of the axial flow velocity, v_a . It then maintains a somewhat constant value throughout the blade before falling to 0 value drastically, just like the axial counterpart.

5.1.3 Induced axial velocity in the propeller plane vs far downstream in the slipstream

The following Fig.5.3 shows the slipstream produced by a propeller disk from propeller plane up till far downstream of the slipstream.

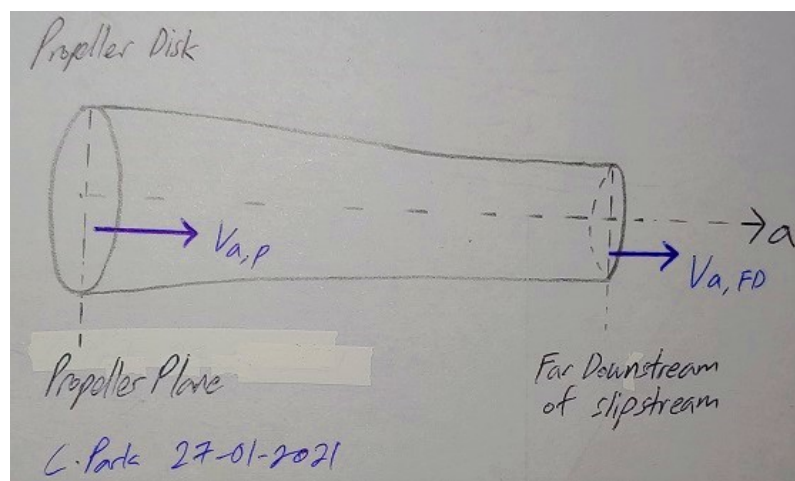


Fig. 5.3 Propeller disk slipstream

When air flows through the propeller plane, it experiences an increase in static pressure and a tangential acceleration whereas the axial velocity remains constant. As this flow moves downstream of slipstream, the flow expands while the static pressure gradually decreases as it is converted into axial velocity and this expansion process reduces the diameter of the slipstream tube as shown in Fig.5.3 [23]. Thus, there is an increase in axial velocity downstream the slipstream. By solving the integral of the difference in pressure over the propeller surface, the thrust generated by the propeller can be calculated as shown in(5.1) given by [24]. The thrust can also be calculated using axial momentum equation shown in (5.2), also given by [24]. The thrust in terms of difference in pressure over the propeller surface is

$$T = \int_{r_p=0}^{R_p} (p_d - p_u) 2\pi r_p \, dr_p \quad (5.1)$$

where T is thrust, r_p is radial position in propeller plane, R_p is outside radius of propeller, p_d and p_u are the pressure downstream and upstream of propeller respectively. As for the thrust from the axial momentum equation, it is

$$T + \int_{r_s=0}^{R_s} (p_\infty - p_s) 2\pi r_s \, dr_s = \int_{r_s=0}^{R_s} (V_{as} - V_\infty) \rho V_{as} 2\pi r_s \, dr_s \quad (5.2)$$

where r_s and R_s are radial position and outer radius of far downstream of slipstream respectively, p_∞ is freestream pressure, p_s is pressure far downstream of slipstream, V_{as} is axial velocity far downstream of slipstream, V_∞ is freestream velocity and ρ is the air density.

Solving and equating these two equations, it was found that the induced axial velocity far downstream, V_{as} (indicated as $V_{a,FD}$ in Fig.5.3), is twice the induced axial velocity in the propeller plane, $V_{a,P}$ [24][25].

5.1.4 Definitions used for propeller characteristics

The following Table 5.1 defines the definitions used in this assignment

Table 5.1 Definitions for propeller characteristics

Parameter	Symbol
Thrust coefficient	C_T
Torque coefficient	C_Q
Power coefficient	C_P

5.1.5 Short explanations

Prandtl Tip Loss Factor

The Prandtl tip loss factor is a correction, derived by Prandtl in 1921, applied to the Blate Element Method (BEM) to take into account the assumption of an infinite number of blades for which the propeller is represented as a disk. It is done to more closely represent a real propeller with a finite number of blades. Four parameters are evaluated for the Prandtl tip loss factor [26] and they are namely:

- Radius related to the distance between the helical wake sheets
- Radius related to the tangential velocity
- Axial induction factor
- Tangential induction factor

Radial flow (Himmelskamp) effect for propellers

Himmelskamp (1947) proposed that the augmentation of aerodynamic load on propeller blades was due to the combination of centrifugal and Coriolis forces. As the centrifugal forces act on the boundary layer of the rotating propeller blades, it enlarges this boundary layer, thus resulting in a larger propeller disk radius.

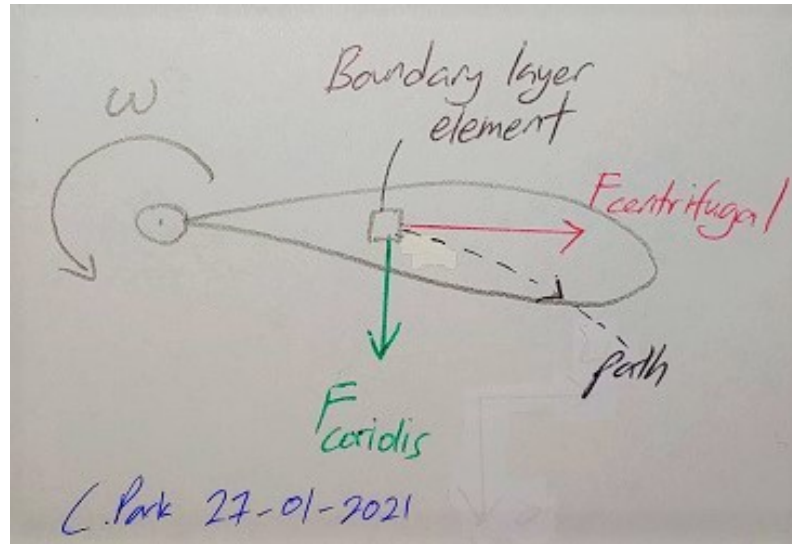


Fig. 5.4 Himmelskamp effect on a boundary layer element of a propeller blade

If an element of the boundary layer is to maintain its chordwise position, it would have a tangential acceleration due to centrifugal force, $F_{\text{centrifugal}}$ and it is opposed by the Coriolis force, F_{coriolis} that pulls the element of the boundary layer towards the trailing edge as shown in Fig.5.4. The Coriolis force then acts as a favourable pressure gradient which results in a delay of the flow separation. Thus, the stall is delayed and the propeller blades can achieve higher maximum lift. This effect is further extended at a lower radial position (thus near the rotational axis of the propeller disk).

Propeller advance ratio

The propeller advance ratio, J , is a non-dimensional parameter that describes the rotational speed of the propeller and it is given by the following equation

$$J = \frac{V_\infty}{nD} \quad (5.3)$$

where V_∞ is the freestream velocity, n is the propeller's rotational speed in the number of revolutions per unit time and D is the diameter of the propeller.

It is said that with increasing in advance ratio, J , the angle of attack, α , at the local blade section decreases for a given pitch angle, β , and vice versa [27]. This is clearly proven by Fig.5.1 whereby an increase in J at a given n and D also increases the freestream velocity, V_∞ , according to (5.3). This increase in V_∞ then causes the angle of attack, α to decrease as shown in Fig.5.1.

5.2 Part 2: Analysis of a propeller

5.2.1 Propeller chosen

For the propeller analysis, propeller 6623-A at blade angle of 15 degrees featured in NACA report number 650 was taken as the experimental data to be used for comparison against the Blade Element Method (BEM) [28]. This propeller features 3 blades and has a diameter of 10 feet,

which is equivalent to 3.048m. The blades sections feature NACA 4400 series airfoil with varying thickness along with the radial locations and this thickness distribution is provided in [28] alongside pitch and chord length distribution. The ratio of hub radius to propeller radius is approximately $R_{hub}/R = 0.28$.

5.2.2 Comparison between BEM and experimental results

The program for BEM has been adapted from the given sample code and it is shown in section 5.3.1. Prandtl tip loss and hub loss correction factors were added which are shown in (5.4) as given by [29]. B represents the number of blades which in this case is 3, R is the radius of the propeller, r is the radial location of the blade element, R_{hub} is the radius of the hub and ϕ is the flow angle.

$$\begin{aligned} F_{total} &= F_{tip} \times F_{hub} \\ F &= \frac{2}{\pi} \cos^{-1} e^{-f} \\ f_{tip} &= \frac{B}{2} \frac{R - r}{r \sin \varphi} \\ f_{hub} &= \frac{B}{2} \frac{r - R_{hub}}{r \sin \varphi} \end{aligned} \quad (5.4)$$

Additionally, it is to be noted that the radial effect which is also known as the Himmelskamp effect that was discussed in section 5.1.5 was note taken into account in the program due to lack of literature available on implementation of the effect into BEM.

The following Fig. 5.5 up till Fig.5.8 show the behaviour of thrust coefficient C_T , torque coefficient C_Q , power coefficient C_P and propeller efficiency η with respect to advance ratio J .

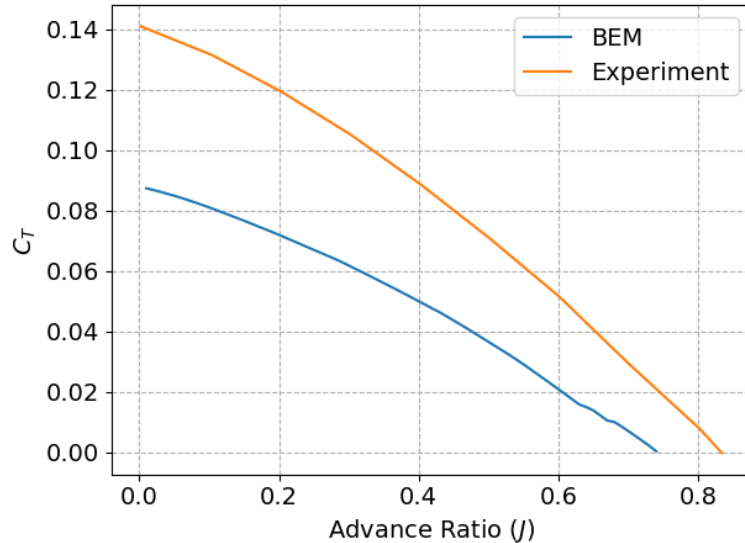


Fig. 5.5 Thrust coefficient vs. advance ratio

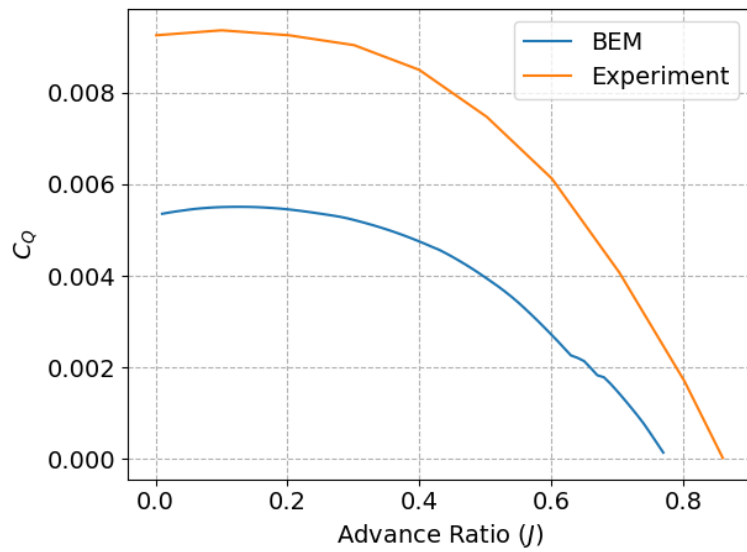


Fig. 5.6 Torque coefficient vs. advance ratio

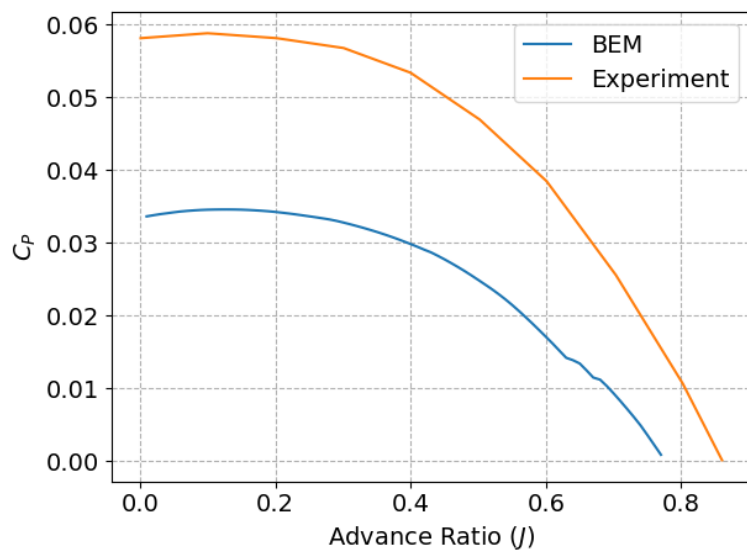


Fig. 5.7 Power coefficient vs. advance ratio

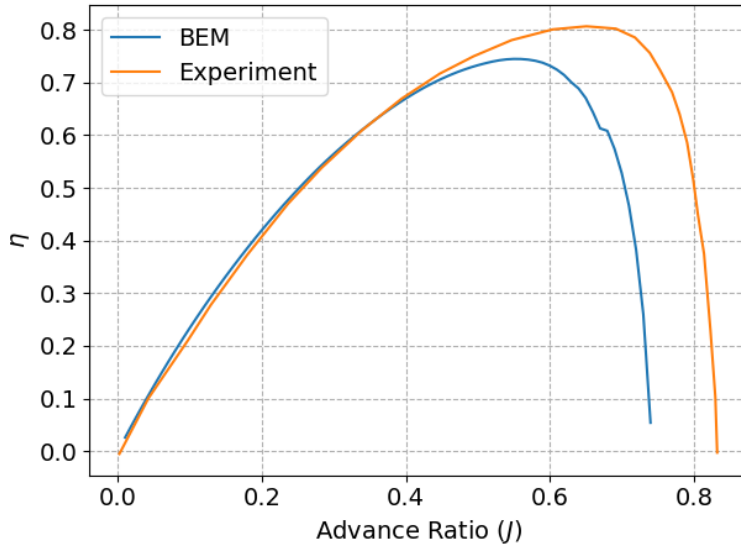


Fig. 5.8 Propeller efficiency vs. advance ratio

It can be observed that for all four plots, the BEM manages to replicate the shape of the experimental data provided by [28] to a large extent. However, there is a certain amount of spacing between the two sets of results for each plot.

Starting with the Fig.5.5, the curve of BEM is shifted down from the curve of experimental results. This could be because the Himmelskamp effect was not implemented into the BEM program. As aforementioned in section 5.1.5, this effect allows for a delay in stall for the propeller blades which leads to an increase in maximum lift. Since the lift contributes largely to the thrust, the exclusion of the Himmelskamp effect has led to the reduction in thrust and hence the shifted down curve that is observed.

This effect is on thrust is also transferred over to torque and power as they are also affected by the magnitude of lift generated by the propeller blade. Thus, Fig.5.6 and Fig.5.7 display almost identical shifted down behaviour from their respective experimental results.

Lastly, for the efficiency η shown in Fig.5.8, it is observed that the maximum is reached much earlier compared to the experimental results. This is due to the thrust, torque and power coefficients reaching a value of 0 at a lower advance ratio J compared to the experimental results which lead to the drastic drop in efficiency.

Additionally, the NACA 4400 series airfoil used for the propeller blade feature specific leading edge and trailing edge radius on top of the standard shape. This was unable to be taken into account due to limitations of designing airfoils in XFLR5 program, which was used to provide lift and drag coefficients of the iterated angle of attacks α of the blade elements in the program. Thus, the values of lift and drag coefficients used would not be perfectly representative of the real behaviour.

5.2.3 Axial velocity distribution

The axial velocity of the propeller blade for a thrust level of $C_T = 0.05$ has been produced as shown in Fig.5.9.

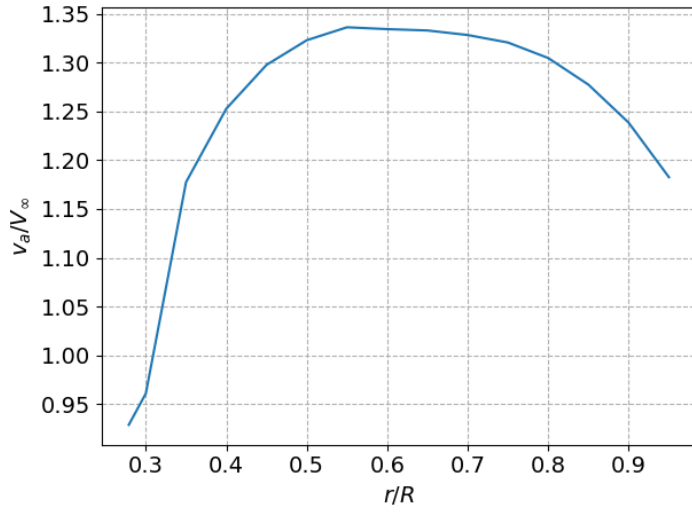


Fig. 5.9 Axial velocity distribution

Majority of the loading is applied on r/R between 0.4 and 0.9. This coincides with Fig.5.2 which shows a similar behaviour of the induced axial velocity from the propeller hub to the tip. This behaviour can be explained with the presence of the hub at which there is no axial velocity present. The hub also affects the blade elements close to it due to the flow restriction and it is the reason for the low value of axial velocity near $r/R = 0.28$, which is equivalent to R_{hub}/R . As the location of blade element moves away from the hub, the axial velocity increases until $r/R = 0.55$ approximately where the maximum efficiency is reached. It then decreases as it nears the propeller tip due to the tip loss and this coincides with the behaviour of Fig.5.2.

5.2.4 Effect of geometrical changes on efficiency

Fixed thrust setting

For a fixed thrust setting of $C_T = 0.05$, the magnitude of radius R and the number of blades B have been varied. The efficiencies of each settings were then obtained and plotted as shown in Fig.5.10 and Fig.5.11.

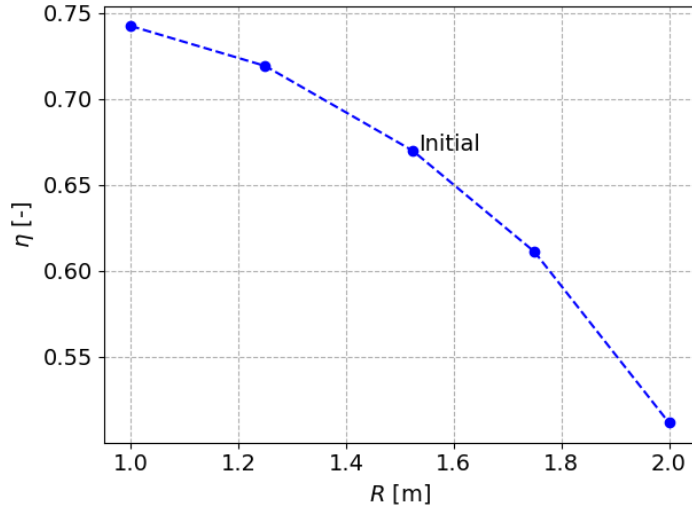


Fig. 5.10 Efficiency vs. radius for fixed thrust setting

It can be observed that the value of efficiency is inversely related to the the radius. With an increase in value of radius, the efficiency decreases. Thus, the smallest radius calculated, $R = 1.0\text{m}$ is the most efficient in this case

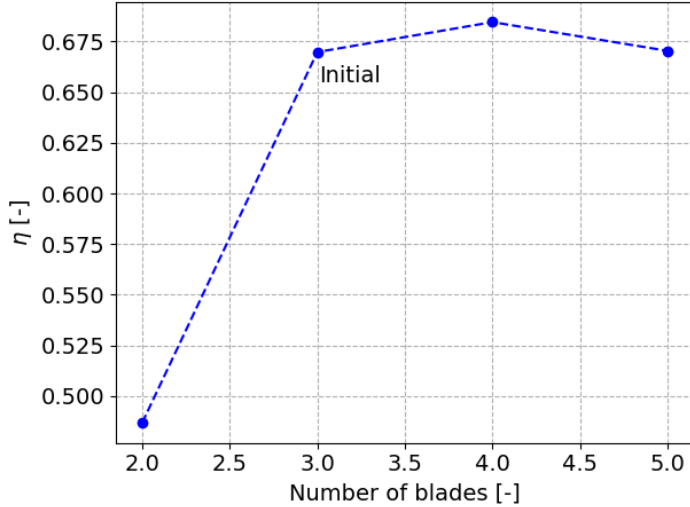


Fig. 5.11 Efficiency vs. number of blades for fixed thrust setting

As for the variance of the number of blades, the change from 3 to 2 blades decreases the efficiency significantly. However, the increase from 2 to 3 only slightly increases the efficiency. Another point at 5 blades was calculated to observe behaviour in further increase. The efficiency did not increase further but instead dropped slightly.

Fixed power setting

The power setting was fixed at $C_P = 0.02$ and the behaviour of efficiency η with respect to change in the value of radius and number of propeller blades were calculated and produced as shown in Fig.5.12 and Fig.5.13.

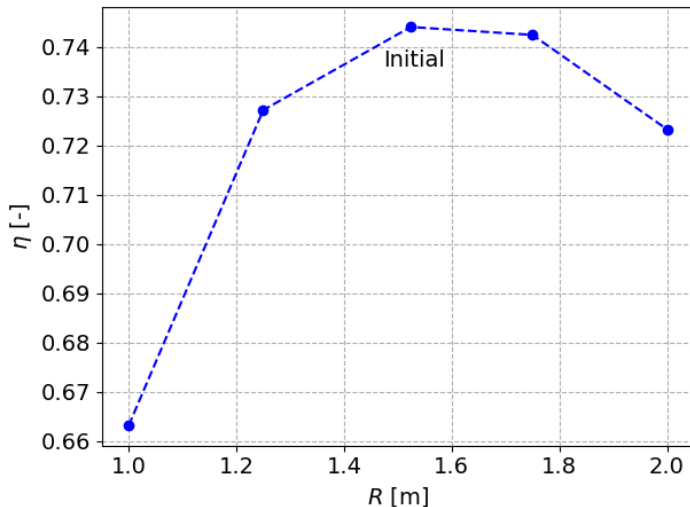


Fig. 5.12 Efficiency vs. radius for fixed power setting

Unlike the trend shown for fixed thrust setting, the efficiency does not strictly decrease with

increasing radius in this case. Instead, both decreasing or increasing the radius from the initial value decreases the efficiency. Thus, the initial value of radius can be said to be optimal.

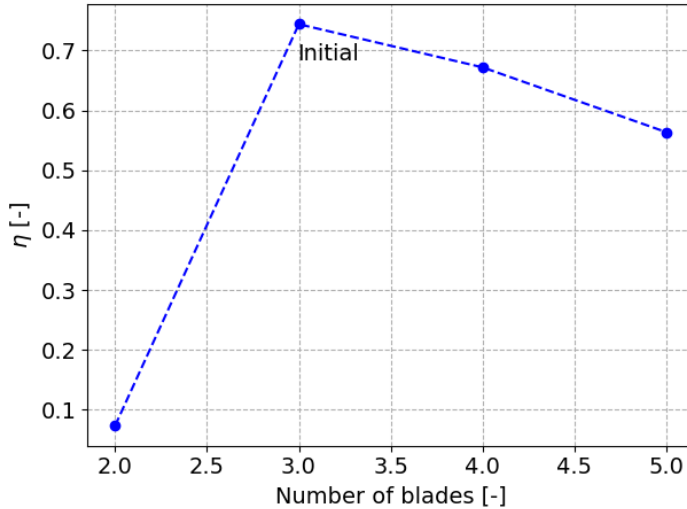


Fig. 5.13 Efficiency vs. number of blades for fixed power setting

Again, it can be observed that the initial number of blades is the optimal value, with the maximum efficiency occurring at this value. Decreasing from 3 to 2 drastically decreases the efficiency to approximately 0.1 whereas increasing from 3 to 4 and 5 gradually decreases the efficiency, but also at a significant amount.

In all, when the power setting is fixed, it is clearly shown that the efficiency is maximum at the initial setting of radius and number of blades. However, this is not apparent for the analyses done for the fixed thrust setting.

5.3 Source code used for the assignment

5.3.1 Blade Element Method for propeller 6623-A

```
1 import matplotlib
2 import numpy as np
3 import pandas as pd
4 import matplotlib.pyplot as plt
5 from scipy.optimize import fsolve
6 from scipy.interpolate import interp1d
7 from matplotlib import rcParams, cycler
8 from math import sqrt, pi, atan, atan2, sin, cos, exp, acos, radians, degrees
9
10 ''' NACA Report 650 - propeller 6623-A at beta 15deg - NACA 4400 series airfoil
11 '''
12 def propdata(filename):
13     df = pd.read_csv(filename, header = None)
14     df = df.to_numpy()
15     x = df[:,0]
16     y = df[:,1]
17     return x, y
18
19 def polardata(filename):
20     df = pd.read_csv(filename, header = 0)
21     df = df.to_numpy()
22     alpha = df[:,0]
23     coeff = df[:,1]
24     return coeff, alpha
25
26 # Interpolate obtained lift/drag polar to find value at specific AOA
27 def interp_alpha(j, alpha_need, coeff):
28     filename = 'polarcsv/sec' + str(j+1) + '-' + coeff + '.csv'
29     coeff, alpha = polardata(filename)
30     # Entire range of AOA does not converge thus find nearest if outside domain
31     if alpha_need < np.min(alpha):
32         coeff_need = coeff[0]
33     elif alpha_need > np.max(alpha):
34         coeff_need = coeff[-1]
35     else:
36         func = interp1d(alpha,coeff)
37         coeff_need = func(alpha_need)
38     return coeff_need
39
40 # correction factor F from ftip/fhub (smallf)
41 def func_F(smallf):
42     return 2/pi * acos(exp(-1*smallf))
43
44 # convert inches to metres
45 def in_m(inches):
46     return inches * 0.0254
47
48 # convert feet to metres
49 def ft_m(ft):
50     return ft * 0.3048
51
```

```

52 # radial dimensions of blade
53 chord_data = propdata("propdata/b_D-new.csv")
54 pitch_data = propdata("propdata/p_D-new.csv")
55 thick_data = propdata("propdata/h_b-new.csv")
56
57 # experimental data
58 ct_exp = propdata("propdata/ct-exp.csv")
59 cp_exp = propdata("propdata/cp-exp.csv")
60 eta_exp = propdata("propdata/eta-exp.csv")
61
62 # fix J
63 V = 51.4096
64 maxJ = 0.9
65 J_arr = np.arange(0.01, 0.9001, 0.01)
66 # number of blades
67 B = 3
68 # diameter of the propeller
69 dia = ft_m(10)
70 # tip radius
71 R = dia / 2
72 # hub radius
73 Rhub = 0.2788 * R
74 # standard sea level atmosphere density
75 rho = 1.225
76 # blade segments
77 pt1 = 0.2788 # r/R=0.2788 is the first point
78 r1 = np.hstack(([pt1],np.arange(0.3, 0.95001, 0.05))) * R
79 # set empty arrays
80 t = np.zeros((np.size(J_arr)))
81 p = np.zeros((np.size(J_arr)))
82 q = np.zeros((np.size(J_arr)))
83 eff = np.zeros((np.size(J_arr)))
84 # convert ratios to actual values
85 chord_arr = chord_data[1] * dia      # variable chord
86 pitch_arr = pitch_data[1] * dia      # variable pitch
87 thick_arr = thick_data[1] * chord_arr # variable thickness (used in polar
→ analysis for airfoil design)
88
89 for i in np.arange(np.size(J_arr)):
90     J = J_arr[i]
91     n = V / J / dia
92     omega = n*2*pi
93     # initialise sums for each velocity
94     thrust = 0
95     torque = 0
96     # loop over each blade element
97     for j in range(0,np.size(r1)):
98         rad = r1[j]
99         # calculate local blade element setting angle
100        pitch = pitch_arr[j]
101        theta = atan(pitch / (2*pi*rad))
102        # calculate solidity
103        chord = chord_arr[j]
104        sigma = B* chord / (2*pi*rad)
105        # guess initial values of inflow (a) and swirl (b) factor
106        a = 0

```

```

107     b = 0
108     # set logical variable to control iteration
109     finished = False
110     # set iteration count and check flag
111     sum = 1
112     ''' iteration for derivates '''
113     while not finished:
114         # axial velocity
115         V0 = V*(1+a)
116         # disk plane velocity
117         V2 = omega*rad*(1-b)
118         # flow angle
119         phi = atan2(V0,V2) # [radians]
120         # blade angle of attack
121         alpha = theta-phi # [radians]
122
123         cl = interp_alpha(j, degrees(alpha), 'cl')
124         cd = interp_alpha(j, degrees(alpha), 'cd')
125
126         # local velocity at blade
127         Vlocal = sqrt(V0*V0+V2*V2)
128         # loss factors
129         ftip = B/2 * (R-rad) / (rad*sin(phi))
130         Ftip = func_F(ftip)
131         fhub = B/2 * (rad-Rhub) / (rad*sin(phi))
132         Fhub = func_F(fhub)
133         Ftot = Ftip * Fhub
134
135         # thrust gradient
136         DtDr = 0.5*rho*Vlocal*Vlocal*B*chord*(cl*cos(phi)-cd*sin(phi))*Ftot
137         # torque gradient
138         DqDr =
139             ↵ 0.5*rho*Vlocal*Vlocal*B*chord*rad*(cd*cos(phi)+cl*sin(phi))*Ftot
140
141         tem1 = DtDr/(4.0*pi*rad*rho*V*V*(1+a))
142         tem2 = DqDr/(4.0*pi*rad**3*rho*V*(1+a)*omega)
143
144         anew=0.5*(a+tem1)
145         bnew=0.5*(b+tem2)
146         # check for convergence
147         if (abs(anew-a)<1.0e-5):
148             if (abs(bnew-b)<1.0e-5):
149                 finished = True
150
151         # update values of a and b
152         a = anew
153         b = bnew
154         # increment iteration count
155         sum=sum+1
156
157     if j == 0: # first element has a different rstep
158         rstep = pt1/2 + 0.05/2
159     else:
160         rstep = 0.05
161
162     thrust = thrust + DtDr * rstep
163     torque = torque + DqDr * rstep

```

```

162
163     t[i]      = thrust / (rho*n*n*dia**4)
164     q[i]      = torque / (rho*n*n*dia**5)
165     p[i]      = 2*pi*q[i]
166     eff[i]    = J_arr[i] / 2 / pi * t[i] / q[i]
167
168     ''' plotting '''
169     plot = True
170     if plot == True:
171         rcParams.update({'font.size': 14})
172
173     fig, ax = plt.subplots()
174     ax.plot(J_arr[J_arr<0.75],eff[J_arr<0.75], label = 'BEM')
175     ax.plot(eta_exp[0], eta_exp[1], label='Experiment')
176     ax.set_xlabel(r'Advance Ratio ($J$)')
177     ax.set_ylabel(r'$\eta$')
178     ax.legend()
179     ax.grid(linestyle='--')
180     fig.tight_layout()
181
182     fig1, ax1 = plt.subplots()
183     ax1.plot(J_arr[t>=-0.00001],t[t>=-0.00001], label='BEM')
184     ax1.plot(ct_exp[0], ct_exp[1], label= 'Experiment')
185     ax1.set_xlabel(r'Advance Ratio ($J$)')
186     ax1.set_ylabel(r"$C_T$")
187     ax1.legend()
188     ax1.grid(linestyle='--')
189     fig1.tight_layout()
190
191     fig2, ax2 = plt.subplots()
192     ax2.plot(J_arr[p>=-0.00001],p[p>=-0.00001], label='BEM')
193     ax2.plot(cp_exp[0], cp_exp[1], label= 'Experiment')
194     ax2.set_xlabel(r'Advance Ratio ($J$)')
195     ax2.set_ylabel(r"$C_P$")
196     ax2.legend()
197     ax2.grid(linestyle='--')
198     fig2.tight_layout()
199
200     cq_exp = cp_exp[1] / 2 / pi
201     fig3, ax3 = plt.subplots()
202     ax3.plot(J_arr[q>=-0.00001],q[q>=-0.00001], label='BEM')
203     ax3.plot(cp_exp[0], cq_exp, label= 'Experiment')
204     ax3.set_xlabel(r'Advance Ratio ($J$)')
205     ax3.set_ylabel(r"$C_Q$")
206     ax3.legend()
207     ax3.grid(linestyle='--')
208     fig3.tight_layout()

```

References

- [1] Jack Moran. *An Introduction to Theoretical and Computational Aerodynamics*. Ed. by Courier Corporation. 2003.
- [2] Joseph Katz and Allen Plotkin. *Low speed aerodynamics*. Ed. by Cambridge University Press. 2001.
- [3] NASA Langley Research Center. “2DN00: 2D NACA 0012 Airfoil Validation Case”. In: (2020). URL: https://turbmodels.larc.nasa.gov/naca0012_val.html.
- [4] Advisory Group for Aerospace Research and Development. *Report of the fluid dynamics panel*. Tech. rep. North atlantic treaty organization, 1979.
- [5] Sighard F. Hoerner. *Fluid-Dynamic Lift*. Ed. by Hoerner Fluid Dynamics. 1992.
- [6] L.L.M. Veldhuis. *Aircraft Aerodynamics, A Primer, Part 2*. Lecture notes. 2020.
- [7] P. R. Owen and L. Klanfer. *On the Laminar Boundary Layer Separation from the Leading edge of a Thin Aerofoil*. Tech. rep. 1955.
- [8] Mark Drela and Harold Youngren. *XFOIL 6.9 User Primer*. 2001.
- [9] Jr. W.C. Lyons and Z. J. Levenstains. “The determination of critical roughness height for boundary layer transition”. In: (1962).
- [10] SKYbrary. *Slats*. 2017. URL: <https://www.skybrary.aero/index.php/Slats>.
- [11] HavKar. *Aircraft High Lift Devices*. 2018. URL: <http://havkar.com/en/blog/view/aircraft-high-lift-devices/99>.
- [12] C.P. van Dam. “The aerodynamic design of multi-element high-lift systems for transport airplanes”. In: *Progress in Aerospace Sciences* 38 (2002).
- [13] A. M. O. Smith. “High-Lift Aerodynamics”. In: *J. Aircraft* (1975).
- [14] Phillip J. Ansell Brent W. Pomeroy Jeffrey M. Diebold and Michael S. Selig. “Study of Burst Wakes in a Multi-Element Airfoil Flowfield”. In: *AIAA Journal* (2014).
- [15] F. W. Spaid V. D. Chin D. W. Peters and R. J. McGhee. “Flowfield measurements about a multi-element airfoil at high Reynolds number”. In: *AIAA Journal* (1993).
- [16] W. H. Wentz, Jr. and H. C. Seetharam. “Development of a flower flap system for a high performance general aviation airfoil”. In: *NASA contractor report* (1974).
- [17] Hepperle M. *JavaFoil 2.27*. 2017.
- [18] Hepperle M. *JavaFoil User’s Guide*. 2017.
- [19] M.M. Munk. “The minimum induced drag of aerofoils”. In: *NACA Report 121* (1921).
- [20] L.L.M. Veldhuis. *Aircraft Aerodynamics Primer part 5*. 2020.
- [21] The Engineering Toolbox. *U.S. Standard Atmosphere*. 2003. URL: https://www.engineeringtoolbox.com/standard-atmosphere-d_604.html.
- [22] Pauli Virtanen et al. “SciPy 1.0: Fundamental Algorithms for Scientific Computing in Python”. In: *Nature Methods* 17 (2020), pp. 261–272. DOI: 10.1038/s41592-019-0686-2.
- [23] G.J.D. Zondervan. *A Review of Propeller Modelling Techniques Based on Euler Methods*. 1998. ISBN: 1111111111.
- [24] W. F. Phillips. “Propeller momentum theory with slipstream rotation”. In: *Journal of Aircraft* 39.1 (2002), pp. 184–187. ISSN: 15333868. DOI: 10.2514/2.2914.
- [25] By R Smedts. “Fixed pitch propeller performance Prediction and analysis using CFD”. In: (2015).
- [26] S F Ramdin. “Prandtl tip loss factor assessed”. In: (2017), p. 180.
- [27] Iván Herráez et al. “Detailed analysis of the blade root flow of a horizontal axis wind turbine”. In: *Wind Energy Science* 1.2 (2016), pp. 89–100. ISSN: 23667451. DOI: 10.5194/wes-1-89-2016.

- [28] R.H. Oppermann. “National advisory committee for aeronautics”. In: *Journal of the Franklin Institute* 226.2 (1938), pp. 231–233. ISSN: 00160032. DOI: 10.1016/s0016-0032(38)90451-x.
- [29] M. K. Rwigema. “Propeller blade element momentum theory with vortex wake deflection”. In: *27th Congress of the International Council of the Aeronautical Sciences 2010, ICAS 2010* 1 (2010), pp. 727–735.